ADVANCES IN INORGANIC CHEMISTRY, VOL. 38

DENSITY-FUNCTIONAL THEORY OF SPIN POLARIZATION AND SPIN COUPLING IN IRON–SULFUR CLUSTERS

LOUIS NOODLEMAN and DAVID A. CASE

Department of Molecular Biology, The Scripps Research Institute,
La Jolla, California 92037

I. Introduction

A variety of metalloproteins have been characterized with active sites containing ligand-bridged transition metal centers that are used for electron transfer and catalysis (*1*). Iron–sulfur proteins provide excellent examples of these types of systems (*2*), as does nitrogenase (*3*), which contains both Fe–S and Mo–Fe–S clusters in a multiple-protein system. Other such electron transfer enzymes include cytochrome oxidase (*4*) and the oxygen-evolving complex of photosystem II (containing a polynuclear Mn–O cluster) (*5, 6*). In the category of substrate transformations, aconitase is a well-known member of a large class of dehydratases with an Fe–S cubane active site (*7*). From an electronic structure viewpoint, common features of all of these clusters include high-spin transition metal centers that are spin coupled via bridging and terminal ligands (*1, 8, 9*). The catalytic and electron transfer repertoires of these clusters can be quite broad, and often have important features that are not seen with single-metal sites. In this review we summarize recent progress toward the development of a unified picture of the electronic structures and spin interactions of iron–sulfur and related systems; these concepts provide a close connection between a spin Hamiltonian description and a more detailed orbital picture of the electron distribution.

The iron–sulfur proteins and synthetic analogs are challenging systems for quantum mechanical methods, both because they contain a large number of electrons and because spin polarization (*10, 11*) and spin coupling (*8, 12–14*) are essential features of the complexes. Standard approaches of *ab initio* quantum chemistry start from a spin-restricted picture, which is poorly adapted to problems involving high-spin transition metal centers (*15*). For this reason, we have developed a combination of broken symmetry and spin-unrestricted methods that is particularly well adapted to study spin-polarized and spin-coupled systems. Further, these ideas are well adapted for use with density-functional methods (*12–14*). In Section II, we develop the basic ideas of this approach, using a perturbation theory formalism to rationalize the spin Hamiltonian and energy-splitting formulas that should be appropriate for spin-coupled transition metal clusters. The basic approach parallels that of "textbook" explanations of superexchange (*16*) and double exchange (*17, 18*), but we consider aspects of the problem not often developed elsewhere.

The perturbation approach is useful in identifying the origins of ferromagnetic and antiferromagnetic interactions, and for developing interpolation formulas for calculating energy differences between spin states. For relatively simple problems, such as the singlet–triplet splitting in dinuclear copper sites, it can also be useful in a computational sense (*19–22*). For coupling problems as complex as iron–sulfur clusters, however, the limitations of perturbation or configuration interaction approaches become severe. Our broken symmetry method, however, can be applied in *ab initio* (*23–25*) as well as in density-functional theory, although so far the computational complexity has constrained *ab initio* methods to smaller systems. In Section III, we outline an alternative, density-functional approach to this problem, which provides a tractable computational *ansatz* for quantitative studies of realistic clusters. In Section IV, spin polarization effects in monomeric iron–sulfur complexes are examined. In Section V, we provide a fair amount of detail for the "worked-out example" of dinuclear iron–sulfur clusters in both the Fe(III)–Fe(III) and Fe(III)–Fe(II) oxidation states. We intend Sections II–V to provide a reasonably self-contained outline of our basic theoretical goals and techniques.

Section VI reviews results of this approach for three-iron (3Fe) iron–sulfur clusters. Section VII contains a review of previous results on 4Fe iron–sulfur clusters, new results on relaxation effects on oxidation and reduction, and an examination of results on spin state equilibria, including some new ideas about $S = \frac{1}{2}$ versus $S = \frac{3}{2}$ ground states. In Section VIII, after a summary of important areas of progress, we look to the future and outline studies in progress on understanding the oxidation/reduction potentials and the ligand-exchange chemistry of these fascinating systems.

II. Perturbation Formalism for Spin Coupling in Transition Metal Clusters

A. OVERVIEW

It is typical to describe the coupling between high-spin transition metal centers in terms of a (phenomenological) Heisenberg Hamiltonian: for two coupled sites, we have $H = J\mathbf{S}_1 \cdot \mathbf{S}_2$ (*22, 26, 27*). As we show in this section, the Heisenberg, or isotropic, coupling model can be derived in a physically interesting way from second-order perturbation theory (*19, 22, 26–29*). One starts from noninteracting high-spin transition metal sites, and then allows for the mixing of "charge transfer" configurations in which the formal oxidation states of the metals are no longer equivalent. In this process, various terms make significant contributions, the most important of which are as follows (*19, 26–29*):

1. *Direct exchange:* this enters already in zeroth order, because there is an exchange interaction between sites even in the absence of charge transfer. The molecular version of Hund's rule ensures that orthogonal orbitals on different centers have the lowest energy in a parallel spin alignment. This interaction is thus ferromagnetic and of Heisenberg type.
2. *Superexchange:* here the metal sites interact by the overlap of opposite spins on neighboring sites. These mainly metal orbitals may contain a ligand part. In a configuration interaction language based on purely orthogonal orbitals, this is equivalent to mixing of charge transfer configurations with the principal configuration. These terms are antiferromagnetic and of Heisenberg type.
3. *Ligand spin polarization:* single-electron (or double-electron) transfers from the doubly occupied ligand orbitals to the high-spin metal sites produce a number of coupling terms of approximately Heisenberg type, which are usually antiferromagnetic (*20, 21, 29*). These terms have often been neglected, but can certainly be important for the types of complexes considered here.
4. *Resonance delocalization* (also called valence delocalization, or double exchange): this arises in mixed-valence situations from the degenerate mixing of equivalent (or nearly equivalent) ionic configurations. The original theory is due to Anderson and Hasegawa (*30*), following Zener (*31*), wherein it was applied to the apparent ferromagnetism of mixed-valence manganites of perovskite structure. The energy of delocalization of the itinerant electron of a mixed-valence pair in a spin-coupled system is given by $\pm|B|(S' + \frac{1}{2})$ for bonding $(-)$ and antibonding $(+)$ interactions, respectively, where S' is the spin quantum number for the coupled pair of sites (*13, 17, 30, 32–36*). In general, both Heisenberg terms and resonance coupling terms are present in mixed-valence complexes, and a key qualitative feature of iron–sulfur clusters is the competition between Heisenberg terms (which are predominantly antiferromagnetic and favor small values of the net spin) and resonance delocalization (which favors high spin values).

B. Singlet–Triplet Splittings for Two Unpaired Electrons

Here we develop a picture of the basic interactions we expect in transition metal clusters, along the lines outlined above. The theory for a system with only two unpaired electrons is especially simple, and we begin with that (*37, 38*). Consider a single configuration wavefunction, defined as an antisymmetrized product of spin orbitals:

$$A[\psi_1(x_1)\psi_2(x_2)\cdots\psi_N(x_N)] = A[u_1(r_1)u_2(r_2)\cdots u_N(r_N)\Theta(s_1, s_2\cdots s_N)] \quad (1)$$

where A is the antisymmetrizing operator. The factorization into space and spin parts is very convenient. Any single configuration wavefunction represents a state with a well-defined spin quantum number $M_S = \langle S_z \rangle$, the expectation value of the z component of total spin, given by $M_S = (N_\alpha - N_\beta)/2$. However, such a wavefunction is not necessarily an eigenfunction of the total spin S, that is, of the operator $\mathbf{S}\cdot\mathbf{S}$. In general, a pure-spin eigenfunction is obtained if all the spin parts of the orbitals are α or all are β outside a closed shell, but not otherwise. For example, consider an open shell composed of two orthogonal space orbitals a, b with opposite spins

$$\Psi_B = A(ab\alpha\beta) \equiv |ab\alpha\beta| \quad (3)$$

Following common practice, the coordinate labels can be omitted, with the convention that the labels increase from left to right. The function Ψ_B is not an eigenfunction of S. Proper spin eigenfunctions $\Psi(S, M_s)$ (*37*) are given by

$$\begin{aligned} \Psi(1,1) &= |ab\alpha\alpha|, \qquad \Psi(1,-1) = |ab\beta\beta| \\ \Psi(1,0) &= 1/\sqrt{2}(|ab\alpha\beta| + |ab\beta\alpha|) \\ \Psi(0,0) &= 1/\sqrt{2}(|ab\alpha\beta| - |ab\beta\alpha|) \end{aligned} \quad (4)$$

from elementary spin algebra. Therefore,

$$\Psi_B = 1/\sqrt{2}[\Psi(1,0) + \Psi(0,0)] \quad (5)$$

The state Ψ_B has $M_S = 0$, but it is not an eigenstate of spin. Rather, it is a state of mixed spin (with both $S = 1$ and $S = 0$ contributing) and will be of broken spatial symmetry if $a(r) \neq b(r)$.

In general, a mixed-spin, broken symmetry state takes the form (*15, 38*)

$$\Psi_B = \sum_S C(S)\Psi_S \quad (6)$$

The "true" electron Hamiltonian of a many-electron system cannot mix eigenfunctions of different spin (in the absence of spin–orbit coupling), and since the total spin operator squared $\mathbf{S}^2$ commutes with this Hamiltonian, we have the energy equation for the broken symmetry state (*15, 38*):

$$E_B = \langle\Psi_B|H|\Psi_B\rangle = \sum_S [C(S)]^2 \langle\Psi_S|H|\Psi_S\rangle \quad (7)$$

There are no cross-terms here between states of different S.

To evaluate the energy of the singlet ($S = 0$) and triplet ($S = 1$)

states, we need also a separate equation for $S = 1$. Keeping always with energy evaluations involving only single configuration wavefunctions,

$$E(S = 1) = \langle\Psi(1,1)|H|\Psi(1,1)\rangle = \langle\Psi(1,-1)|H|\Psi(1,-1)\rangle \qquad (8)$$

Note that we have chosen not to make use of $\Psi(1,0)$ since this has more than one configuration. There is nothing "wrong" with multiconfigurational wavefunctions, but local density-functional theory (as we discuss below) is most easily given a concrete and well-defined form in terms of single configuration wavefunctions (*15, 38*).

The energy of the broken symmetry wavefunction in the present case is now easily found:

$$E_B = (\tfrac{1}{2})[E(S = 0) + E(S = 1)] \qquad (9)$$

Of more interest is the singlet–triplet splitting:

$$E(S = 1) - E(S = 0) = 2[E(S = 1) - E_B] \equiv J \qquad (10)$$

where J is the Heisenberg parameter in a Hamiltonian of the form $H = J\mathbf{S}_1 \cdot \mathbf{S}_2$. Equation (10) has been used for many years to estimate singlet–triplet splittings in molecular excited states using Xα or local density-functional theory. The above derivation is of course a very simple one, but we will see that the basic concepts carry through to more complex situations; only the algebra becomes more complicated.

C. NONORTHOGONAL ORBITALS

So far, we have assumed that the space orbitals $a(r)$ and $b(r)$ are orthogonal, that is

$$\int a(r)b(r)\,dr \equiv S_{ab} = 0 \qquad (11)$$

This will be true in many molecular excited states wherein the orbitals may be orthogonal by symmetry. For the case of coupling of two transition metal ions, it may be approximately true if the coupling is weak. Hund's rule implies that the coupling will be ferromagnetic ($J < 0$) when a and b are orthogonal, but it can be either ferromagnetic or antiferromagnetic when a and b are nonorthogonal. We now consider the more general situation for nonorthogonal orbitals (e.g., valence bond orbitals) a', b' with overlap $S_{a'b'}$. Then it may be shown that the corresponding broken symmetry wavefunction is (*15, 39*)

$$\Psi_B = [(1 + S^2_{a'b'})/2]^{1/2}\,\Psi(0,0) + [(1 - S^2_{a'b'})/2]^{1/2}\,\Psi(1,0) \qquad (12)$$

The corresponding energy equation is (*15, 39*)

$$E(S = 0) = [2/(1 + S^2_{a'b'})]E_B - [(1 - S^2_{a'b'})/(1 + S^2_{a'b'})]E(S = 1) \qquad (13)$$

For small $S_{a'b'}$, this reduces to Eq. (10); as $S_{a'b'} \rightarrow 1$, we have the strong bonding limit, in which the broken symmetry state approaches the singlet state [Eq. (12)]. The two-electron valence bond problem is thus solvable throughout the entire range of $S_{a'b'}$. Taking the difference $J = E(S = 1) - E(S = 0)$ from Eq. (13) gives the singlet–triplet splitting solely in terms of $E(S = 1)$, E_B, and the overlap $S_{a'b'}$. These results have been used effectively together with density-functional calculations to evaluate the singlet–triplet splitting and electronic structure in (d^9–d^9) copper dimer and (d^9–d^1) copper–vanadium dimer complexes in both the strong bonding and weak bonding regimes (*40–43*). Some of these are copper dimer peroxide complexes having structural relevance to the active sites of hemocyanin and tyrosinase (*40*).

D. INTERACTIONS OF MORE THAN TWO ELECTRONS

However, when more than two unpaired electrons are weakly coupled, the complete problem is not solvable; substantial progress can be made through recourse to perturbation theory (*28, 29*). Consider a single configuration wavefunction (determinant) in which both spin and space symmetry restrictions have been lifted. For a dinuclear metal cluster, this would have nonorthogonal "magnetic orbitals" $d'_\mathrm{l}, d'_\mathrm{r}$, mainly on the metal centers (where l and r denote the left and right transition metal centers), and nonorthogonal ligand orbitals $l^{k'}\alpha, l^{k''}\beta$, including both the bridging and terminal ligands. Typically, this single configuration wavefunction would be variationally optimized as a broken symmetry unrestricted Hartree–Fock or local density-functional wavefunction. This wavefunction can be expanded in terms of determinants built upon *orthogonal* orbitals (*28, 29*):

$$\Psi_B = |[d'_\mathrm{l}][\alpha\alpha\alpha\cdots][l^{k'}l^{k''}][\alpha\beta][d'_\mathrm{r}][\beta\beta\beta\cdots]| = D_0 + \sum_u a_u(B)D_u \qquad (14)$$

The excited configurations D_u are created by excitations from the principal determinant D_0, and the $a_u(B)$ are mixing coefficients in the expansion of the broken symmetry state Ψ_B. The principal determinant D_0 is built from orthogonalized metal and ligand orbitals:

$$D_0 = |[d_\mathrm{l}][\alpha\alpha\alpha\cdots][l^k l^k][\alpha\beta][d_\mathrm{r}][\beta\beta\beta\cdots]| \qquad (15)$$

For simplicity, D_0 is assumed to be orbitally nondegenerate, and with n unpaired electrons on the left of spin α, n unpaired electrons on the right of spin β, and with doubly occupied ligand orbitals on the bridging and terminal ligands with space part l^k. (Formally, doubly occupied d orbitals can be treated in way analogous to doubly occupied ligand orbitals.)

Through a corresponding orbital transformation (*44, 45*) the nonorthogonal orbitals d' can be made to overlap only in pairs, so that $\langle d'_{\mathrm{l}u} | d'_{\mathrm{r}v} \rangle$ vanishes unless $u = v$. In terms of the normalized orthogonal orbitals d_l and d_r, we then have $d'_{\mathrm{l}u} = d_{\mathrm{l}u} + a_u(B) d_{\mathrm{r}u}$, $d'_{\mathrm{r}u} = d_{\mathrm{r}u} + a_u(B) d_{\mathrm{l}u}$, and $\langle d'_{\mathrm{l}u} | d'_{\mathrm{r}u} \rangle = 2a_u(B)$. This provides a relationship between the mixing coefficients in the orthogonal representation [Eq. (14)] and the magnetic orbital overlaps in the nonorthogonal representation (*26, 28*). Thus, interactions such as superexchange can often be described equally well in terms of orbital overlap or configurational mixing, and both descriptions are common in the literature. The magnetic orbitals are partly delocalized onto the bridging and terminal ligands, as well as onto the opposite metal center. The overlaps $\langle d'_{\mathrm{l}u} | d'_{\mathrm{r}u} \rangle$ often strongly involve the bridging ligands, so that their contribution to spin coupling is called superexchange (*26, 27, 46*). Similarly, the nonorthogonal ligand orbitals $l^{k'}, l^{k''}$ can be expanded as a doubly occupied set plus a small deviation due to delocalization onto the neighboring metal site(s) (*20, 29*). The contribution of the latter to spin coupling is called ligand spin polarization, or "hole" polarization. Each of these mechanisms can lead to spin transfer from the metal to the ligands.

To treat the states of pure spin, we recognize that each determinant in Eq. (14) is like an "outer product" of monomer spins. The Clebsch–Gordan algebra can be used to express this in terms of the spin eigenstates of the coupled system (*47–49*):

$$|S_1 M_1\rangle |S_2 M_2\rangle = \sum_S C(S_1 S_2 S; M_1 M_2) |SM\rangle \tag{16}$$

where C is a Clebsch–Gordan coefficient. In the principal determinant D_0, there are n unpaired electrons on the left and right, and the two spin vectors $S_1 = S_2 = n/2$ are coupled to total spin S; for superexchange, the relevant excited state configurations D_u arise from $d_\mathrm{l} \rightarrow d_\mathrm{r}$ or $d_\mathrm{r} \rightarrow d_\mathrm{l}$ excitations that leave $n - 1$ unpaired electrons per site, so that $S_1 = S_2 = \frac{1}{2}(n - 1)$; for ligand spin polarization, the excited configurations arise from $l^k \rightarrow d_\mathrm{l}$ or $l^k \rightarrow d_\mathrm{r}$ excitations, again with $S_1 = S_2 = n/2$. Hence, there are two important types of coupling coefficients, $C_1(S) \equiv [C(\frac{1}{2}n\ \frac{1}{2}nS; \frac{1}{2}n\ -\frac{1}{2}n)]$ and $C_2(S) \equiv \{C[\frac{1}{2}(n - 1)\ \frac{1}{2}(n - 1)S; \frac{1}{2}(n - 1)\ -\frac{1}{2}(n - 1)]\}$.

Combining Eqs. (14) and (16) then yields an expression for the broken symmetry state in terms of spin eigenstates:

$$\begin{aligned}\Psi_B &= \sum_S C_1(S)\,\Phi_0(S) + \sum_S\sum_u a_u(B)C_u(S)\,\Phi_u(S)\\ &= \sum_S C_1(S)\left\{\Phi_0(S) + \sum_u [a_u(B)C_u(S)/C_1(S)]\,\Phi_u(S)\right\}\end{aligned}\tag{17}$$

where Φ represents the appropriate spin-coupled state $|SM\rangle$, and $C_u(S)$ will be $C_2(S)$ for determinants of the superexchange type and $C_1(S)$ for ligand spin polarization excitations. The quantity in brackets is nearly $\Psi(S)$, the wavefunction that would be generated by spin projection on Ψ_B, followed by variational optimization (*28, 29*). This equivalence is exact for excitations of the superexchange type, and is approximate (but expected to be fairly accurate) for ligand spin polarization (*29*). This has the fortunate consequence that a variational optimization of Ψ_B followed by spin projection [the construction followed for each term in brackets in Eq. (17)] yields results nearly as accurate as those obtained by constructing the proper spin states first, and then performing the variational optimization, a more accurate but difficult procedure. As with Eqs. (6) and (7), we can then write:

$$\Psi_B = \sum_S C_1(S)\Psi(S) \tag{18}$$

$$E_B \equiv \langle\Psi_B|H|\Psi_B\rangle = \sum_S C_1(S)^2\,\langle\Psi(S)|H|\Psi(S)\rangle \equiv \sum_S C_1(S)^2 E_S \tag{19}$$

These expressions contain an important (and perhaps surprising) result: that both the broken symmetry wavefunction and its energy can be connected in a simple way to pure spin states. This forms the foundation for the application of the Wigner–Eckart theorem to the calculation of spin properties (to be discussed in Sections V and VII) and for the estimation of spin state energetics, which we discuss next.

The second main ingredient in our approach to spin coupling involves the development of an expression for E_S. Since we have already alluded to the use of a Heisenberg Hamiltonian, it may seem natural to expect E_S to be proportional to $S(S + 1)$, but it is important to note that this is a consequence of our theoretical picture of transitional metal clusters and not just a convenient assumption. A justification for the Heisenberg form for the pure spin states has been given in several earlier papers (*13, 28, 29*), and here we only have space for an outline of the argument.

The basic ideas can be illustrated by considering the effects of spin projection on the principal determinant D_0, Eq. (*15*). Let O_S be the projection operator onto the subspace of spin S; then applying Eq. (16) as before, we can write:

$$O_S D_0 = C_1(S)\,\Phi_0(S) = [C_1(S)]^2 \sum_v X_v(S) D_0^v \tag{20}$$

In the second equation, we recognize that spin projection will result in a mixture of determinants D_0^v arising from interchanges of spin indices from the sets $[d_l]$ and $[d_r]$. The coefficient $X_v(S)$, where $v = (ij)$, represents the substitution $(d_l^j\alpha \rightarrow d_l^j\beta,\ d_r^i\beta \rightarrow d_r^i\alpha)$ turns out to have the form (*50–52*)

$$X_{(ij)}(S) = -\{[n - S(S + 1)]/n^2\} \tag{21}$$

and the coefficient for the principal determinant, X_0, is just unity. Then the energy of the spin-projected state is

$$\langle\Phi_0(S)|H|\Phi_0(S)\rangle = \langle D_0|H|D_0\rangle + E^{(1)}(S) \tag{22}$$

where

$$E^{(1)}(S) = \{[n - S(S + 1)]/n^2\} \sum_{ij} \langle d_l^j d_r^i | r_{12}^{-1} | d_r^i d_l^j\rangle \equiv -[n - S(S + 1)]J_F/2 \tag{23}$$

Since the spin-dependent portion goes like $S(S + 1)$, the result is of Heisenberg form, and the final equality in Eq. (23) defines J_F, the ferromagnetic Heisenberg parameter for a "direct exchange" interaction. Since the exchange integrals in Eq. (23) are positive definite, J_F must be negative (ferromagnetic) so that orthogonal orbitals on the two centers have the lowest energy for parallel spin alignment.

The effects of spin projection on the matrix elements for the excited determinants D_u follows a similar, although algebraically more complex, path. It turns out that for the superexchange excitations, the spin states also fit the Heisenberg form, but with an exchange parameter J_{AF} that is predominantly positive (antiferromagnetic) (*28*). The ligand spin polarization terms lead to energies that have a Heisenberg component plus terms of order $[S(S + 1)]^2$; the latter terms would correspond to a spin Hamiltonian $J_q(S_1 \cdot S_2)^2$, but are expected to be smaller than the Heisenberg contributions (*29*).

The above considerations motivate us to adopt the *ansatz* that the E_S values are of Heisenberg form with $E_S = S(S + 1)J/2$, where $J = J_F + J_{AF}$. The Clebsch–Gordan algebra also allows one to directly show that (*28*)

$$\sum_{S=0}^{S_{\max}} C_1(S)^2 S(S + 1) = n = S_{\max} \tag{24}$$

Combining Eqs. (19) and (24) yields an expression for the energy difference between two single configuration states, that of S_{max} and the broken symmetry state:

$$E(S_{\mathrm{max}}) - E_B = (S_{\mathrm{max}}^2 J/2) \tag{25}$$

where $J = (J_{\mathrm{F}} + J_{\mathrm{AF}})$. This is the principal result of this section, since (as we discuss below) it is computationally tractable to estimate the energies of single configuration states. Note that Eq. (10) is a special case of this relation, with $S_{\mathrm{max}} = 1$.

E. Analysis of a Mixed-Valence Dimer

When an electron is added to form the reduced dimer, the resulting energy terms are of two types. First, there are Heisenberg terms that originate from direct exchange, superexchange, and ligand spin polarization, analogous to those in the preceding discussion. In addition, there are resonance delocalization interactions resulting from the mixing of the degenerate configurations created by the (arbitrary) assignment of the extra electron to the left or right side of the system (*13, 30*).

It is easiest to characterize the principal and excited functions by their vector coupling structure. Consider an outer product spin state of the form $|S_1 M_1\rangle_{\mathrm{L}}\,|S_2 M_2\rangle_{\mathrm{R}}$, where L and R are the left and right metal centers. The principal spin configuration is $|\frac{5}{2}\ \frac{5}{2}\rangle_{\mathrm{L}}\ |2\ -2\rangle_{\mathrm{R}}$, with the electron added to side R. Excited configurations of superexchange type can be included by methods analogous to those in the previous section. These terms lead to a Heisenberg Hamiltonian for the pure spin states and to the corresponding energy difference equation (*13, 28*)

$$E(S_{\mathrm{max}}) - E_B = n(n-1)J/2 \tag{26}$$

for the broken symmetry state, compared with the pure spin state energy difference:

$$E(S_{\mathrm{max}}) - E(S = \tfrac{1}{2}) = (n+1)(n-1)J/2 \tag{27}$$

Resonance delocalization terms have a different character entirely (*13*). To see this, consider the principal determinant wherein an electron is added to the metal site on the right of the dimer. Then the normalized principal determinant is

$$D_{0\mathrm{R}} = |[d_{1\mathrm{L}} \cdots d_{5\mathrm{L}}][\alpha^5][d_{1\mathrm{R}} d_{1\mathrm{R}}][\alpha\beta][d_{2\mathrm{R}} \cdots d_{5\mathrm{R}}][\beta^4]| \tag{28}$$

Now $D_{0\mathrm{R}}$ is the outer product state $|\tfrac{5}{2}\ \tfrac{5}{2}\rangle_{\mathrm{L}}\ |2\ -2\rangle_{\mathrm{R}}$, so that we can use the Clebsch–Gordan algebra of Eq. (16) to write it in terms of spin eigenstates:

$$D_{0\mathrm{R}} = \sum_{S} C(\tfrac{5}{2}\, 2S; \tfrac{5}{2}\ -2)\Phi_{0\mathrm{R}}(S) \tag{29}$$

Applying the spin projection operator O_S to both sides, and rearranging,

$$\Phi_{0\mathrm{R}}(S) = O_S D_{0\mathrm{R}}/C_a(S) \tag{30}$$

where $C_a(S) \equiv C(\tfrac{5}{2}\, 2S; \tfrac{5}{2}\ -2)$. A similar equation holds for spin projection of $D_{0\mathrm{L}}$. Then the resonance matrix element of the spin-projected states can be written:

$$\begin{aligned}\langle\Phi_{0\mathrm{L}}(S)|H|\Phi_{0\mathrm{R}}(S)\rangle &= [C_a(S)]^{-2}\langle O_S D_{0\mathrm{L}}|H|O_S D_{0\mathrm{R}}\rangle \\ &= [C_a(S)]^{-2}\langle D_{0\mathrm{L}}|H|O_S D_{0\mathrm{R}}\rangle\end{aligned} \tag{31}$$

In the second line, we have made use of the fact that O_S is idempotent (so that projection only needs to be done once).

Now we note [as in Eq. (20)] that the effect of spin projection on $D_{0\mathrm{R}}$ will again be to mix in other determinants $D_{0\mathrm{R}}^{p}$ in which spin indices have been interchanged:

$$O_S D_{0\mathrm{R}} = C_a(S)\Phi_{0\mathrm{R}}(S) = C_a(S)\sum_{p} z_p D_{0\mathrm{R}}^{p} \tag{32}$$

There is only one non-vanishing term in the sum, so that

$$\langle\Phi_{0\mathrm{L}}(S)|H|\Phi_{0\mathrm{R}}(S)\rangle = [C_a(S)]^{-1} z_{p'}\langle D_{0\mathrm{L}}|H|D_{0\mathrm{R}}^{p'}\rangle \tag{33}$$

The important determinant is the one that nearly matches $D_{0\mathrm{L}}$, except that one of the R orbitals, $d_{1\mathrm{R}}\beta$, appears in the determinant where the matching L orbital, $d_{1\mathrm{L}}\beta$, appears in $D_{0\mathrm{L}}$:

$$D_{0\mathrm{R}}^{p'} = |[d_{1\mathrm{R}} \cdots d_{5\mathrm{R}}][\alpha^5][d_{1\mathrm{L}}d_{1\mathrm{R}}][\alpha\beta][d_{2\mathrm{L}} \cdots d_{5\mathrm{L}}][\beta^4]| \tag{34}$$

$$D_{0\mathrm{L}} = |[d_{1\mathrm{R}} \cdots d_{5\mathrm{R}}][\alpha^5][d_{1\mathrm{L}}d_{1\mathrm{L}}][\alpha\beta][d_{2\mathrm{L}} \cdots d_{5\mathrm{L}}][\beta^4]| \tag{35}$$

Note further that $D_{0\mathrm{R}}^{p'}$ is a determinant in the expansion of the state function $|\tfrac{5}{2}\ -\tfrac{3}{2}\rangle_{\mathrm{L}}\ |2\ 2\rangle_{\mathrm{R}}$, so that the coefficient $z_{p'}$ will involve the Clebsch–Gordan coefficient $C\,(\tfrac{5}{2}\, 2S;\ -\tfrac{3}{2}\ 2) \equiv C_b(S)$; in fact, $z_{p'} = C_b(S)/(5)^{1/2}$. Thus the spin-dependent part of Eq. (33) becomes $C_b(S)/C_a(S)(5)^{1/2}$. By direct examination of the Clebsch–Gordan coefficients it can be shown that this ratio is $(S + 1/2)/(5)$. Hence we have finally that

$$\langle\Phi_{0\mathrm{L}}(S)|H|\Phi_{0\mathrm{R}}(S)\rangle = B(S + 1/2) \tag{36}$$

where B is a constant of proportionality. Equation (36) is the principal result of this analysis; we discuss below ways in which B can be estimated from single configuration wavefunctions.

F. SUMMARY

There is a lot of algebra in the above exposition, and it may be worthwhile here to summarize the most important results:

1. Most of the contributions (through second order in perturbation theory) to the energies of a transition metal dimer with the same number of d electrons on each site have a spin dependence like that of the Heisenberg spin Hamiltonian, $H = J\mathbf{S}_1 \cdot \mathbf{S}_2$. Some aspects of ligand spin polarization effects have a more complex spin dependence, but these terms are expected to be small.
2. Direct exchange between the magnetic orbitals on the two sites will lead to a ferromagnetic (negative) contribution to J, whereas superexchange interactions will make a contribution that is generally antiferromagnetic. Ligand spin polarization effects will also generally be antiferromagnetic. Each of these contributions can be identified with the mixing of particular sorts of excited configurations into a canonical single-determinant reference state.
3. A broken symmetry, spin-unrestricted wavefunction provides a simple wavefunction that also contains these physical interactions. The broken symmetry solution is not a spin eigenfunction, but can be written as a superposition of spin eigenfunctions, with relatively simple expressions for the weighting coefficients [see Eqs. (16)–(18)]. This implies that the energy of the broken symmetry function can be related to that of the spin eigenstates, Eq. (19), providing a convenient path for obtaining estimates of the Heisenberg coupling constants, Eq. (25). For the mixed-valence case, the Heisenberg coupling constants are found from Eq. (26).
4. For mixed-valence situations, an additional type of interaction arises from the resonance interaction between mirror-image configurations, in which the extra electron is assigned either to the left- or the right-hand metal site. These terms are also expected to have a relatively simple spin dependence, as the product of a "hopping interaction" times the factor $S + \frac{1}{2}$. Mixed-valence clusters also have Heisenberg terms analogous to those in the even-electron clusters, so that the appropriate spin Hamiltonian must contain both Heisenberg and resonance delocalization terms.

III. The Density-Functional and Broken Symmetry Methods

Density-functional methods are an alternative to *ab initio* methods for complex quantum chemical problems (*53*). Compared to *ab initio* methods, the distinctive feature of density-functional theory is that the exchange correlation part of the energy is approximated by terms that depend only on functionals of the electron density (*54, 55*). The use of this approximate form has the advantage of being more efficient than *ab initio* Hartree–Fock methods; for transition metal ions and related complexes, these are also often more accurate than Hartree–Fock calculations, as we discuss below (*53*). Spin-polarized density functional theory is analogous to unrestricted Hartree–Fock (UHF) theory (*13, 15, 28*). Unlike spin-restricted Hartree–Fock theory (RHF), this takes spin-polarized transition metal sites as its starting point. If the overall system is spin coupled to less than the maximal spin alignment, the simplest way to express this is to have different spatial orbitals for the different spin indices, giving a spin-polarized broken symmetry description of the molecule (*12, 13, 28*).

A. THE TOTAL ENERGY IN DENSITY-FUNCTIONAL THEORY

To have a language general enough to encompass both density-functional theory and the quantum mechanical theory of many-electron systems, we begin our analysis with some basic concepts from the theory of reduced density matrices. Our discussion basically follows that of McWeeny and Sutcliffe (*37*), and of Ziegler *et al.* (*38*), but at the end there is an interesting new twist. Let a general coordinate $x = (r,s)$ represent both independent space and spin variables. Let the electrons occupy orbitals $u_{i\alpha}(r)\alpha(s)$ and $u_{i\beta}(r)\beta(s)$ for α and β spins, respectively, with corresponding electron densities $\rho_\alpha(r)$, $\rho_\beta(r)$:

$$\begin{aligned} \rho_\alpha(r) &= \sum_{i\alpha} n_i u_i^*(r) u_i(r) \\ \rho_\beta(r) &= \sum_{i\beta} n_i u_i^*(r) u_i(r) \qquad (37) \\ \rho(r) &= \rho_\alpha(r) + \rho_\beta(r) \end{aligned}$$

where the n_i are orbital occupation numbers.

To formulate the total energy expression in density functional theory, a generalized version of the electron density ρ is needed, called the first-order density matrix:

$$\rho_1(r; r') = \sum_{i=\alpha,\beta} n_i u_i(r) u_i^*(r') \qquad (38)$$

The full first-order density matrix is needed so that the kinetic energy of the system can be defined entirely in terms of expectation values over density matrices. The following expression is then valid even for very complicated correlated wavefunctions:

$$\begin{aligned} E &= \int_{r'=r} [-\nabla^2/2]\rho_1(r;r')\,dr + \int_r \rho(r)V_N(r)\,dr \\ &\quad + \tfrac{1}{2}\int_{x_1,x_2} \rho_2(x_1,x_2)r_{12}^{-1}\,dx_1\,dx_2 + U_{NN} \qquad (39) \\ &= T + V_{Ne} + U_{ee} + U_{NN} \end{aligned}$$

Here the first term (T) is the total kinetic energy of the electronic system, the second term is the nuclear–electron attraction energy (V_{Ne}), the third term is the total electron–electron repulsion energy of the system (U_{ee}), and the last term is the nuclear–nuclear repulsion energy; $\rho_2(x_1, x_2)$ is the diagonal part of the second-order density matrix. The electron–electron repulsion is given by the expectation value of the electron–electron Coulomb repulsion operator r_{12}^{-1} with ρ_2. The use of the generalized space-spin coordinates x_1, x_2 shows that this repulsion includes both that of α spin electrons among themselves, of β spin electrons among themselves, and of α electrons with β electrons. The diagonal part of the second-order density matrix can be separated into four terms involving only the two space variables (r_1, r_2), and spin indices α, β. These are $\rho_2^{\alpha\alpha}$, $\rho_2^{\beta\beta}$, $\rho_2^{\alpha\beta}$, and $\rho_2^{\beta\alpha}$.

For a system in which the total number of electrons is N, we have the following conservation equations

$$\int \rho(r)\,dr = N \qquad (40)$$

$$\int \rho_2(r_1, r_2)\,dr_1\,dr_2 = N(N-1) \qquad (41)$$

Since the conservation equation applies equally to α and β spin electrons, $N_\alpha + N_\beta = N$. The last equation can be interpreted as saying that every electron in the system interacts with all other electrons (but not with itself). The factor of $\frac{1}{2}$ in the U_{ee} equation is required so that every pairwise interaction of electrons is counted only once, giving the number of distinct pairwise interactions as $N(N-1)/2$. We can expand $N(N-1)$ in the following illuminating way:

$$\begin{aligned} N(N-1) &= (N_\alpha + N_\beta)(N_\alpha + N_\beta - 1) \\ &= N_\alpha(N_\alpha - 1) + N_\beta(N_\beta - 1) + N_\alpha N_\beta + N_\beta N_\alpha \qquad (42) \end{aligned}$$

The individual terms on the right-hand side are the integrals of $\rho_2^{\alpha\alpha}(r_1, r_2)$, $\rho_2^{\beta\beta}(r_1, r_2)$, $\rho_2^{\alpha\beta}(r_1, r_2)$, and $\rho_2^{\beta\alpha}(r_1, r_2)$. All α electrons interact with all β electrons, and with the other $N_\alpha - 1$ electrons of the same spin. Further insight into electron–electron interactions comes from comparing correlated and uncorrelated forms of second-order density matrix. Specifically, $\rho_2(r_1, r_2)$ is the joint probability density for finding any electron at r_1 and another at r_2. By contrast, a "classical" (uncorrelated) electron density would give a joint probability distribution

$$\rho_2^{\text{class}}(r_1, r_2) = \rho(r_1)\rho(r_2) \tag{43}$$

Similar relations apply for the α and β densities independently. In the next sections we consider separately the types of correlations expected for electrons of the same spin and of opposite spins.

B. EXCHANGE ENERGY AND THE FERMI HOLE

Clearly, for $\rho_2^{(\alpha\alpha)}$, the equations above dictate that the correct joint probability function deviates substantially from the classical uncorrelated form, since

$$\int \rho_2^{\text{class}(\alpha\alpha)}(r_1, r_2)\, dr_1\, dr_2 = N_\alpha^2 \tag{44}$$

rather than $N_\alpha(N_\alpha - 1)$. The exact quantum mechanical $\rho_2^{(\alpha\alpha)}$ can be expressed in the following form (*37*):

$$\rho_2^{(\alpha\alpha)}(r_1, r_2) = \rho^\alpha(r_1)\rho^\alpha(r_2)[1 + f^{\alpha\alpha}(r_1, r_2)] \tag{45}$$

This result is the sum of an uncorrelated part plus an additional term describing "Fermi correlation." Dividing both sides by $\rho^\alpha(r_2)$ yields the conditional probability for finding an electron of spin α at r_1 given that there is another spin α electron at r_2. Rearranging Eq. (45),

$$[\rho_2^{(\alpha\alpha)}/\rho^\alpha(r_2) - \rho^\alpha(r_1)] = \rho^\alpha(r_1)[f^{\alpha\alpha}(r_1, r_2)] \tag{46}$$

The right-hand side of the equation is the "Fermi hole" density. The integral of this density over r_1 is -1 for any r_2. Further, the Pauli exclusion principle requires that as $r_1 \to r_2$, $f^{\alpha\alpha}(r_1, r_2) \to -1$, so that no two α spin electrons can be at the same place. Thus, electrons of the same spin exhibit "Fermi correlation" in their interactions. For a single configuration wavefunction (an antisymmetrized product of spin orbitals), a Fermi hole with the properties cited above is obtained by construction, leading to the exchange term in the total energy equation. In density-functional theory, the constraints above can be used to obtain a reasonable form for the exchange potential in terms of the electron density. For a uniform electron gas with density ρ, this turns out to have the form $V_X^\sigma = (\frac{2}{3})U_X^\sigma$, where $U_X^\sigma = -(\frac{9}{2})\alpha[\frac{3}{4}\pi)\rho^\sigma]^{1/3}$, where $\sigma = \alpha$ or β spin indices and the prefactor $\alpha = \frac{2}{3}$ for pure exchange and is variable in some other approaches (54, 56). The entire electron–electron repulsion energy (U_{ee}) of the system is approximated by

$$U_{ee} = \tfrac{1}{2}\int \rho(r_1)\rho(r_2)\, r_{12}^{-1}\, dr_1\, dr_2 + \tfrac{1}{2}\int [\rho^\alpha(r_1)U_X^\alpha(r_1) + \rho^\beta(r_1)U_X^\beta(r_1)]\, dr_1 \tag{47}$$

The first integral is the "classical" electron–electron repulsion, and the second is the total exchange energy. A similar philosophy applies for the analysis of correlation effects. The goal is to find an approximate form for U_{XC} (where XC means exchange and correlation) for use in an equation similar to Eq. (47), based, for example, on the exchange and correlation energy of an electron gas (local spin density functional, or LSD) method *(57–60)*, or on gradient corrections to the exchange energy (Becke's energy) *(61)*.

C. CORRELATION FOR OPPOSITE SPINS AND THE COULOMB HOLE

Consider now the joint distribution function for electrons of opposite spin. We can write this in a form similar to Eq. (45) *(37)*:

$$\rho_2^{(\alpha\beta)}(r_1, r_2) = \rho^\alpha(r_1)\rho^\beta(r_2)[1 + f^{\alpha\beta}(r_1, r_2)] \tag{48}$$

but now the "Coulomb hole density" integrates to zero for any r_2:

$$\int \rho^\alpha(r_1) f^{\alpha\beta}(r_1, r_2)\, dr_1 = 0 \tag{49}$$

This follows directly from the fact that the integral of $\rho_2^{(\alpha\beta)}$ is $N_\alpha N_\beta$. The Coulomb hole is not necessarily small, despite the fact that it must integrate to zero over all space. The important physical result is that as $r_1 \to r_2$, $\rho_2^{(\alpha\beta)}(r_1, r_2)$ becomes small so that electrons of opposite spin avoid each other so as to reduce their Coulomb repulsion. The Coulomb hole density is thus negative at short distances and positive at larger distances, to give a zero integral over all space.

As with exchange energies, these opposite-spin correlation effects could be approximated by using an $f^{\alpha\beta}$ function derived for a uniform electron gas, or from explicitly correlated wavefunctions. This is not, however, the only way. Unlike the Pauli principle, which is a precise symmetry requirement for fermions, the Coulomb hole is essentially a means by which a wavefunction can lower its electron–electron repulsion, and also its total energy. One way to achieve this is to remove whatever constraints are keeping the electron–electron repulsion too high. In a standard spin-restricted framework, as, for example, in restricted Hartree–Fock theory, $\rho^{\alpha}(r) = \rho^{\beta}(r) = \rho/2$, and the electron repulsion between α and β electron densities is high. Our alternative is not to focus on $f^{\alpha\beta}(r_1, r_2)$, but instead to change the form of ρ^{α}, ρ^{β} from restricted to unrestricted form, allowing the electron densities for α and β spin to differ in space; how they differ precisely will be determined by the self-consistent field of the system in the density functional calculation. For the individual orbitals, this means removing the constraint that the orbitals be members of the irreducible representations of the molecular point group defined by the nuclear geometry. The orbitals are instead calculated in a subgroup compatible with the symmetries of ρ^{α} and ρ^{β}. By using unrestricted spin orbitals, all of the energy terms (kinetic energy, nuclear electron attraction, and electron–electron repulsion) will change in a variationally optimal way. Both the classical electron–electron repulsion and the exchange energy terms in U_{ee} are altered when passing from the spin-restricted to the spin-unrestricted case. In general, the α and β densities become more compact, and occupy different regions in space. These effects are quite strong when there are spin-polarized transition metal atoms, because the energetic cost on the kinetic energy of having compact α and β densities is outweighed by the advantageous lowering of the electron–electron repulsion and of the spin polarization (exchange) energies. Further, the broken symmetry state and its energy will differ significantly from the high-spin state and its energy, even though both will experience spin polarization, because the two states have different covalency and delocalization, affecting all the energy terms.

IV. Monomeric Iron–Sulfur Complexes

There have been two different types of first-principle calculations on single-iron Fe–S clusters: unrestricted Hartree–Fock plus configuration interaction [on models $Fe(SH)_4{}^{1-/2-}$] (*11*) and spin-polarized (unrestricted) Xα–scattered wave (sw) [on $Fe(SH)_4{}^{1-/2-}$ and $Fe(SCH)_3)_4{}^{1-/2-}$] (*10, 14*). These are in good agreement. The ground state of the models and of oxidized rubredoxin is high-spin $S = \frac{5}{2}$; formally, simple orbital counting gives ferric d^5 for the oxidized complex and ferrous d^6 for the reduced complex. When the orbitals are optimized in the spin-polarized self-consistent field (SCF) procedure, there is extensive mixing of sulfur into the mainly Fe magnetic orbitals, and, conversely, mixing of Fe character into doubly occupied S levels. In the oxidized complex (*10, 14*) there is about a 5-eV splitting between the occupied spin-up Fe(3*d*) orbitals (majority spin orbitals, lower energy) and the unoccupied spin-down Fe(3*d*) orbitals (minority spin orbitals, higher energy), indicative of a large intraatomic exchange splitting. The mainly S(3*p*) levels lie between the two sets of Fe(3*d*) in energy and are also spin split, but by a much smaller amount and in the opposite sense (spin-down below spin-up).

This general level pattern persists in polynuclear iron–sulfur clusters and has strong experimental support in model systems. This level structure, with the S(3*p*) band lying between the exchange-split Fe(3*d*) band, is not found in standard ligand field models (derived from low-spin systems), where all the ligand levels are expected to lie below all the metal levels, and seems to be a general feature of high-spin transition metals in the presence of weak-field ligands such as S. This "inverted bonding scheme" has been established experimentally by Solomon and co-workers (*62–65*) in the monomeric ferric complexes $FeCl_4^-$ and $Fe(SR)_4^-$ by a combination of spectroscopies, including photoelectron spectra (PES), polarized absorption, magnetic circular dichroism (MCD), and EPR. These show that the lowest lying spin-forbidden transitions in the oxidized system have substantial ligand → Fe character and are incompatible with ligand field Fe $d \rightarrow d$ transitions. Their energies are much lower in synthetic $Fe(SR)_4^-$ complexes than in $FeCl_4^-$, consistent with the stronger metal–ligand covalency in the thiolate complex. Resonance PES further establishes that the majority spin Fe(3*d*) lies below S(3*p*) in energy (*62, 63*).

V. Iron–Sulfur Dimers

A. ENERGY LEVEL STRUCTURE

In Fig. 1, we give the energy levels for the broken symmetry (BS) state (low spin, $M_S = 0$) of the dimeric cluster $Fe_2S_2(SH)_4^{2-}$ in C_{2v} symmetry (*13*). The symmetry is lowered from the D_{2h} geometrical symmetry of the cluster by removing the mirror plane through the bridging S* atoms. The energy level structure and orbitals are consistent with antiparallel coupling of two high-spin subunits, each with spin vector $S = \frac{5}{2}$. On the diagram, the orbitals are arranged in columns according to their spatial distribution on the left, center, and right of the molecule, and according to the spin index [solid and dashed lines for spin-up (α) and spin-down (β) orbitals, respectively].

Because this is a homonuclear cluster with a geometrical equivalence

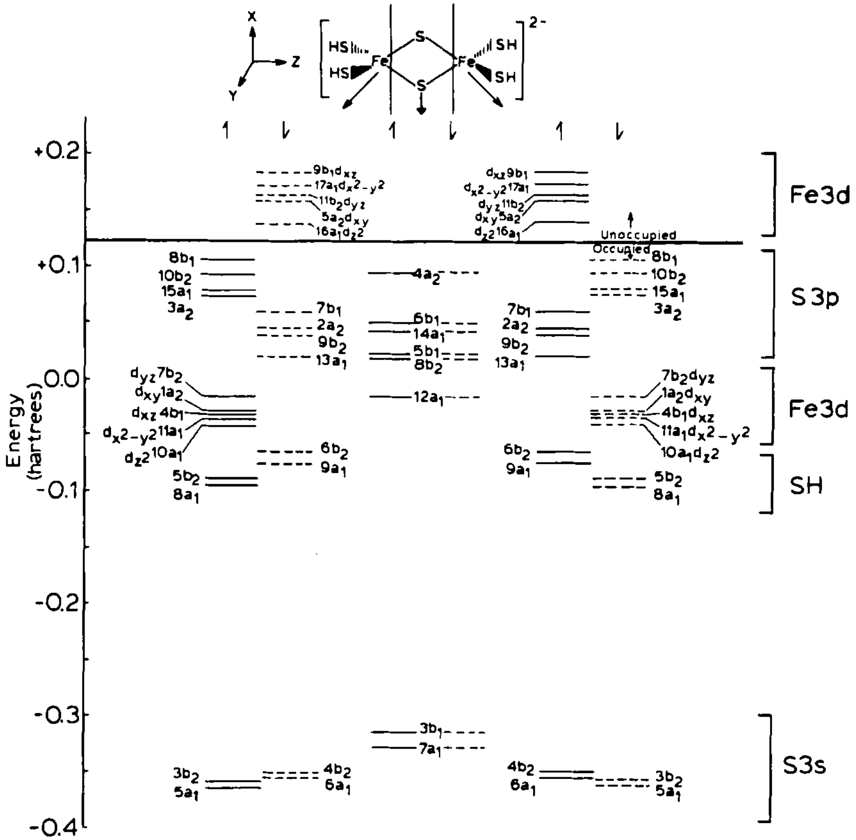

FIG. 1. Xα–LCAO energy levels for $Fe_2S_2(SH)_4^{2-}$; antiferromagnetic configuration. The orbitals are grouped according to their distribution on the left, center, or right of the molecule. Spin-up (α) levels are shown with solid lines, spin-down (β) levels are shown with dashed lines. See Ref. *13*.

between the left and right halves, each spin-up level on the left is energetically degenerate with a mirror-image spin-down orbital on the right. Further, the orbitals can be grouped into a set of spin-up/spin-down pairs with large spatial overlap, mainly on the ligands, and into a set, mainly on the metal atoms where the spin-up/spin-down overlap between occupied orbital pairs is small. For example, $8a_1\alpha$, $9a_1\beta$ are SH bonding orbitals on the left, and $3a_2\alpha$, $2a_2\beta$ are terminal S orbitals. These are essentially "doubly occupied" ligand orbitals, and most of the orbitals in the system are of S, S*, or SR type. In contrast to this are the mainly Fe(3*d*) orbitals, which experience a large intraatomic exchange splitting. The occupied or "magnetic" spin-up Fe(3*d*) orbitals on the left (majority spin) are strongly stabilized by spin polarization and are metal–ligand bonding, whereas the corresponding spin-down Fe(3*d*) orbitals on the left (minority spin) are destabilized and unoccupied. The magnetic orbitals exhibit weak spatial overlap between the occupied spin-up orbitals on the left, largely on $\mathrm{Fe_L}$, and the occupied spin-down orbitals on the right, largely on $\mathrm{Fe_R}$. The weak valence bond (VB) type of interaction between the metal centers can be thought of as a type of very weak M–M covalent bonding, distributed over the five valence bond pairs.

The high-lying S(3*p*) orbitals obey the "inverted bonding scheme" lying between the two parts of the exchange-split Fe(3*d*) band. The terminal S(3*p*) spin splitting (about 1.5 eV) is considerably smaller than that for Fe(3*d*) (about 5 eV), with the terminal S spin-down orbitals lying lower when the neighboring Fe(3*d*) occupied orbitals are spin-up. Energetically, the bridging S*(3*p*) orbitals also appear between the majority-spin and the empty minority-spin Fe(3*d*) levels, resembling the lower S(3*p*) terminal orbitals in energy.

The majority-spin Fe(3*d*) levels are metal–ligand (M–L) bonding. The adjacent terminal S(3*p*) orbitals of opposite spin to the Fe(3*d*) are also primarily of M–L bonding character, which is achieved by mixing with empty Fe(3*d*) atomic orbitals. The S*(3*p*) orbitals behave similarly, while the highest terminal S(3*p*) orbitals are pushed up by antibonding interactions with the adjacent filled Fe(3*d*) levels of the same spin. The greatest Fe–S antibonding interactions occur in the empty ligand field levels; the reduction from tetrahedral Fe site symmetry to C_{2v} splits $e \rightarrow a_1, a_2$, and $t_2 \rightarrow a_1, b_1, b_2$. Overall, the exchange splitting of the Fe(3*d*) band is further enhanced by bonding and antibonding interactions with S(3*p*).

In Fig. 2, we show a contour map of the Fe magnetic orbital $7b_2\alpha$. There is considerable S radical character in $7b_2\alpha$, as well as a small $7b_2\alpha$–$7b_2\beta$ superexchange interaction. Other magnetic orbitals displaying superexchange are shown in Ref. *13*. For example, in the interaction of the magnetic orbitals $10a_1\alpha$ with $10a_1\beta$, superexchange interactions are clearly present since there is metal–ligand as well as metal–metal overlap. Figure 2 also includes a map of a high-lying occupied S(3*p*) orbital, $10b_2\alpha$, and of two ligand field orbitals, $16a_1\alpha$ and $9b_1\alpha$; these are unoccupied Fe(3*d*) orbitals in the oxidized model. On reduction, the added electron goes into $16a_1\alpha$, composed mainly of a localized $\mathrm{Fe}(3d_{z^2})$ orbital.

B. DENSITY DIFFERENCES AND SPIN DENSITIES

Density difference maps for the difference between the molecular electron density of the BS state and that of the spin-restricted atoms

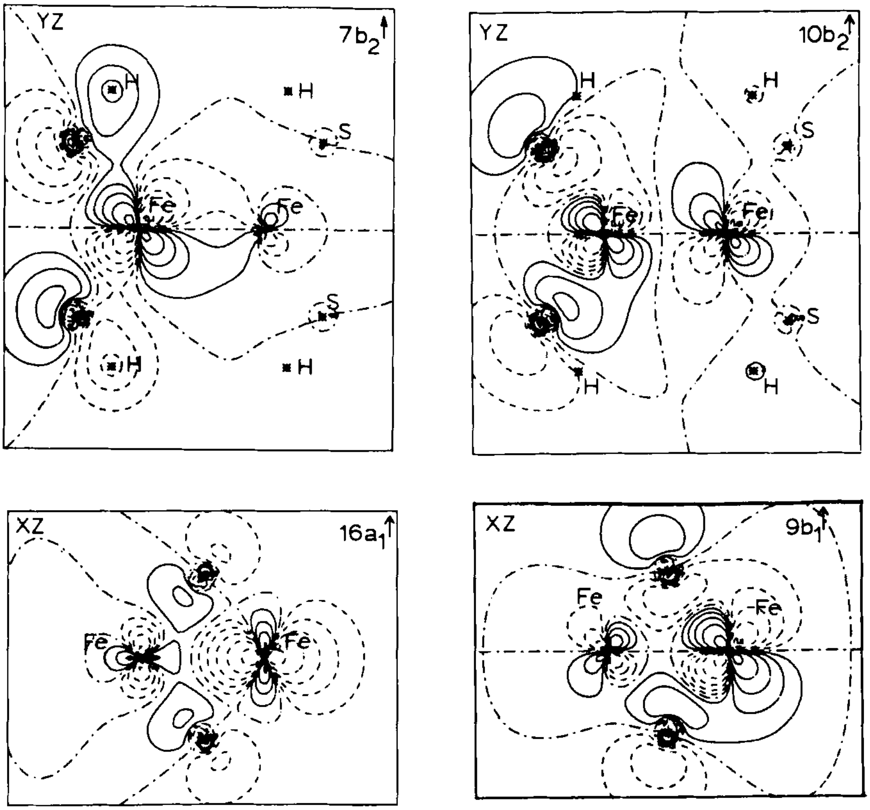

FIG. 2. Contour maps for the orbitals $7b_2$, $10b_2$, $16a_1$, and $9b_1$ spin-up (α) in the Fe–S* bridging (xz) or Fe–SR terminal (yz) plane as indicated for $Fe_2S_2(SH)_4^{2-}$. See Ref. *13*.

clearly show the accumulation of electrons in the bonding region between Fe and S, and in the SH bonds (see Ref. *13*). When compared, the maps of the reduced and oxidized cluster show a complex rearrangement of charge. Occupation of $16a_1\alpha$ produces a substantial increase of axial electron density on the trapped Fe site (right), $0.64e^-$ in the reduced-site Fe($3d_{z^2}$) population. However, electron relaxation through the other "passive" orbitals leads to a large backflow of electron density out of the other reduced-site Fe orbitals; the total Fe($3d$) population increases by only $0.11e^-$ compared with oxidized cluster. The increased electron population in the reduced form has thus gone almost entirely to the sulfurs. Further, the two SH groups (right) adjacent to the reduced Fe site have a larger electron population than two SH (left) by $0.24e^-$. Hence the asymmetry and trapping are preserved at the level of net charge flow, as well as for the orbital occupied on reduction in Ψ_B. These results show the strong participation of the S, S* in the redox process, and demonstrate the importance of metal–ligand covalency.

Spin density maps for Ψ_B in both the oxidized and reduced forms of the cluster are also given in Ref. *13*. For the oxidized cluster, the spin density maps show the strong spin polarization on Fe and the substantial spin transfer from Fe → terminal S. The opposite spin alignment on the two Fe sites is also evident. Upon reduction, the same general picture holds, but with a reduction in the axial spin density on the reduced site (at the right). The relationship of these spin density maps to what is actually observed, for example, in the Fe or proton hyperfine tensors, contains some subtleties. When the $S = 0$ ground state is projected out of the broken symmetry state of the oxidized cluster, the spin density necessarily vanishes. However, the higher states of the spin ladder ($S > 0$) have nonvanishing spin density, which shows up, for example, as paramagnetic shifts in the nuclear magnetic resonance (NMR) of oxidized proteins at the cysteine methylene protons, and in related synthetic clusters (*9, 66*). This opposite spin alignment is also clearly seen in the Fe hyperfine tensors of reduced clusters.

C. HYPERFINE, EPR, AND MÖSSBAUER PROPERTIES FOR REDUCED TWO-IRON CLUSTERS

For the reduced dimer, spin projection of the $S = \frac{1}{2}$ ground state from Ψ_B leads to an effective spin density from which hyperfine properties can be determined (*13*). Let (S_1, M_{S_1}) and (S_2, M_{S_2}) be the monomer subunit spin quantum numbers; for Ψ_B, $M_{S_1} = S_1 = \frac{5}{2}$ and $M_{S_2} = -S_2 = -2$. Next, the properties of the proper $S = \frac{1}{2}$ ground state must be related to those in Ψ_B. From the Wigner–Eckart theorem for vector operators (*49*), the effective **A** tensors are then $\mathbf{A}_{i\,\mathrm{eff}} = K_i\mathbf{a}_i$, where $K_i = \langle \mathbf{S} \cdot \mathbf{S}_i \rangle / S(S+1)$ (so that $K_1 = \frac{7}{3}$, $K_2 = -\frac{4}{3}$), and the $\mathbf{a}_i$ are "site tensors" determined as for monomeric metal complexes (*9, 67*). The analysis of the **g** tensor is similar, with $\mathbf{g} = K_1\mathbf{g}_1 + K_2\mathbf{g}_2$ (*8*). Griffith has shown that the **g** and $\mathbf{A}_{\mathrm{eff}}$ tensors for the total system can be constructed and diagonalized to give principal values and axes, independent of whether the site tensors have the same principal axis system (*68*).

Our **g** and **A** tensor calculations for the $Fe_2S_2^{1+}$ model cluster have been discussed in detail previously (*13, 69–71*). Here we emphasize a few important points. The calculated **g** tensor is rhombic in a principal axis system, with $g_x = 1.87, g_y = 1.96, g_z = 2.01$, where z is the Fe–Fe axis, xz is the 2Fe–2S* bridge plane, and yz is the 2Fe–4(SR) terminal plane as in Fig. 1. These results are in rather good agreement with results for typical reduced plant ferredoxins (such as spinach), $g_x = 1.88, g_y = 1.96, g_z = 2.04$ (*9*), and not in agreement with the axial **g** tensors found in putidaredoxin or adrenal ferredoxins (*67*). The anisotropic parts of the Fe hyperfine tensors show the same behavior, with much better agreement for the plant ferredoxins (*9, 72, 73*). The largest value (magnitude) of the anisotropic part of the **A** tensor on the ferrous site is along the Fe–Fe axis from the theory, consistent with the filling of $16a_1\alpha$ (Fe d_{z^2}). The predicted Mössbauer quadrupole splitting for the reduced site is large and negative ($\Delta E_Q = -3.1$ mm/sec, with principal axis z) (*14*), which is similar to the values measured for reduced plant ferredoxins (*9, 72, 74*). Comparison of our theoretical results for g values with the phenomenological model of Bertrand and Gayda shows similar covalency: orbital reduction factor 76% for the spin–orbit coupling constant (*67*) versus 56 to 75% Fe(3d) character in the unoccupied orbitals $16a_1$ to $9b_1$. The mixing between Fe d_{z^2} and $d_{x^2-y^2}$ is small in $16a_1$ (*13*). When the mixing parameter θ is defined by $|16a_1\rangle = \cos\theta|d_{z^2}\rangle + \sin\theta|d_{x^2-y^2}\rangle$, we find $\theta = 8^0$ for the reduced system [Xα–linear combination of atomic orbitals (LCAO)]. The extent of mixing depends, however, on the orientation of the SR groups; in general, the mixing is larger if the SR groups lie close to the Fe–Fe (z) axis, and smaller (as above) for SR away from the z axis (*13*). Further, the latter case corresponds to a large negative quadrupole splitting with the z principal axis on the ferrous site, whereas the former may have a positive value and/or another principal axis (*14*).

Utilizing the predicted Mössbauer trends above (negative ΔE_Q in algal ferredoxins), and the known X-ray structure of the algal ferredoxin *Spirulina platensis* (*75*), we predicted (*14*) that the reduced site in this ferredoxin should be at Fe Cys 46, Cys 41, since the z direction opposite to Fe–Fe is rather open here, in contrast to Fe Cys 79, Cys 49. This prediction has recently been confirmed by NMR nuclear Overhauser experiments of Dugad *et al.* (*76*).

D. HEISENBERG COUPLING AND RESONANCE COUPLING

To analyze spin coupling, the broken symmetry state Ψ_B with energy E_B must be compared with the high-spin state $\Psi(S_{\max})$ with energy $E(S_{\max})$. In the oxidized system, the broken symmetry state [also referred to as the low-spin and antiferromagnetic (AF) configuration] is described by the energy level structure in Fig. 1; the spin vectors for the monomer subunits are oppositely aligned (*12, 13*). The oxidized high-spin state [or ferromagnetic (F) configuration] is constructed by parallel spin alignment of the monomer spin vectors. The oxidized F state thus has 10 spin-α magnetic electrons and none of spin β; its energy level diagram is the result of an independent SCF calculation for $S = 5$, shown in Fig. 3. The F state has essentially the same D_{2h} symmetry as the nuclear framework, and both the V_α and V_β one-electron potentials have the same symmetry. In Fig. 3, notice that the unoccupied (minority or β) spin orbitals are symmetrically delocalized over both halves of the molecule. These are mainly Fe(3*d*) in character. There is then no barrier to electron delocalization upon reduction for the F state, in contrast to a substantial barrier and localization that we find for the broken symmetry, AF configuration. This is depicted schematically in Fig. 4.

The Heisenberg exchange coupling constant for the oxidized system was evaluated using Eq. (25). In the X-ray structures of 2Fe–2S algal ferredoxins (*75, 77*), at least one axial site is rather open; in all cases, however, the protein structures give a much less symmetric cluster coordination geometry to cysteine S than in our theoretical models. Experimentally, $J_{\text{ox}} = 366$ and 298 cm^{-1} for oxidized spinach ferredoxin (*78*) and for a synthetic analog (*79*). The theoretical values are larger, Xα–LCAO gives $J_{\text{ox}} = 620$ cm^{-1} for an open axial-site model geometry; see Table I (*13*).

For the reduced system, we must consider both the Heisenberg coupling parameter J_{red} and the resonance parameter B in our analysis. For the proper spin eigenstates, we begin with the Heisenberg spin ladder, which is then split by resonance delocalization into g, u components of the form

$$E(S)_{g,u} = JS(S + 1)/2 \pm B(S + \tfrac{1}{2}) \tag{50}$$

For the higher spin eigenstates, the resonance splitting is substantial, and we expect that local asymmetries will not be strong enough to quench the resonance. For the lowest spin states, the resonance splitting is much smaller, and (given that the J coupling is antiferromagnetic) the resonance can be quenched by environmental asymmetries, including the coordination environment, hydrogen bonding, solvation, and vibronic effects.

Our goal is to extract the J_{red} and B parameters from the density-functional calculations and to explore the implications of the results. Figure 5 is a schematic diagram of the Heisenberg plus resonance Hamiltonian. The Heisenberg spin ladder is at the left, and the resonance splitting is shown in the next column. At the right is the corre-

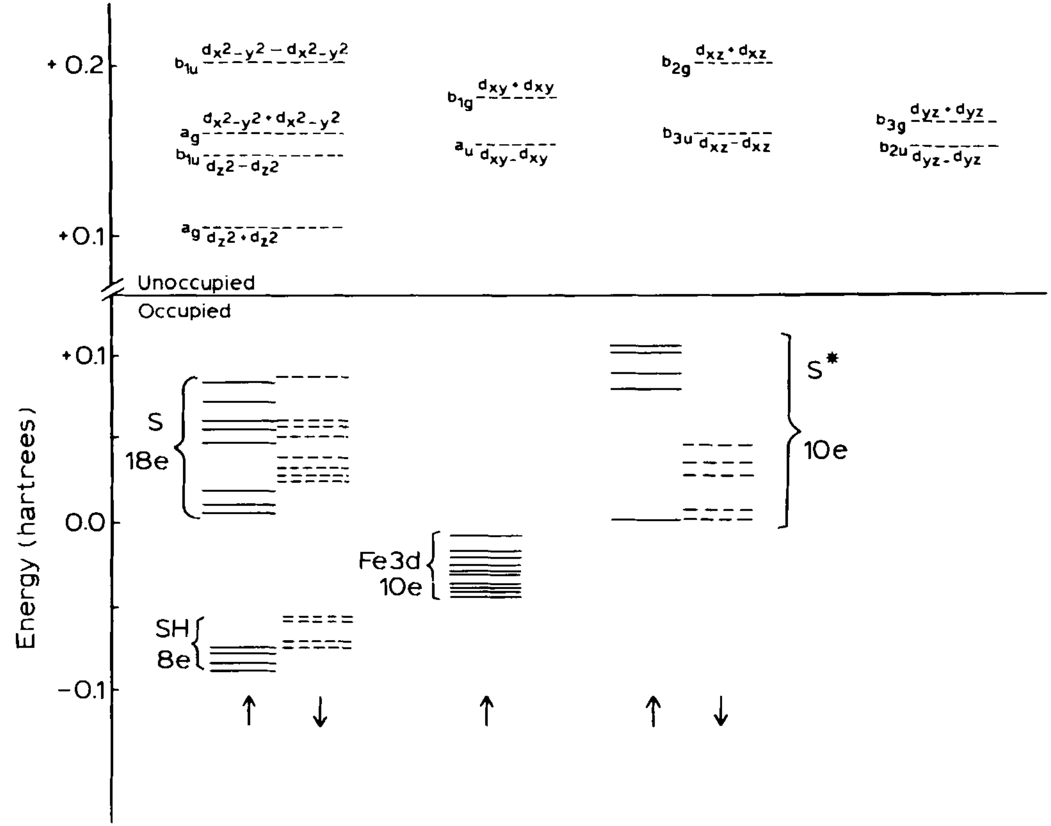

FIG. 3. Xα–LCAO energy levels for high-spin ferromagnetic configuration, $Fe_2S_2(SH)_4^{2-}$. There is an excess of 10 spin-α electrons. The occupied levels are grouped according to orbital character (S, Fe, etc.), and the unoccupied levels are specified by their symmetries in the D_{2h} group and Fe(3*d*) character. See Ref. *13*.

TABLE I

SPIN HAMILTONIAN PARAMETERS[a]

Compound	Geometry	J_{ox}	J_{red}	B'	B	J_{red}/J_{ox}	$\lvert B/J_{red}\rvert$
$Fe_2S_2^{2+/1+}$		620	346		−516	0.56	1.5
$Fe_3S_4^{1+/0}$	Linear	544	407	—	−568	0.75	1.4
$Fe_3S_4^{1+/0}$	Cubane	369	297	−30	−406	0.81	1.4
$ZnFe_3S_4^{3+/2+}$	Cubane	360	282	−28	−407	0.78	1.4
$ZnFe_3S_4^{1+}$	Cubane	—	45	−64	−426	0.16[b]	9.5
$Fe_4S_4^{3+}$	*A*	—	416	—	−722	1.09[c]	1.7
			472	−297	−722	0.96[c]	1.5
$Fe_4S_4^{2+}$	*A*	—	454[d]	—	−740[d]	—	1.6
$Fe_4S_4^{1+}$	*A*	—	231[e]	—	−715[e]	0.51[b]	3.1
			379	−590	−715	0.83[b]	1.9
	B		145	—	−696	0.32[b]	4.8
			300	−622	−696	0.66[b]	2.3

[a] Values in cm^{-1}. Except as noted below, all values are determined from the Xα potential; results for 3Fe clusters are from scattered-wave calculations (*91, 92, 95*), and those for 2Fe and 4Fe clusters are from LCAO expansions (*13, 94*). For the +1 and +3 oxidation states of Fe_4S_4, the upper line gives results for a two-parameter fit in which the interlayer resonance B' is ignored; the lower line gives results for a three-parameter fit in which it is included. For Fe_4S_4, the *A* geometry is taken from model complexes in the +2 oxidation states, and the *B* geometry is from model complexes in the +1 oxidation state; see Ref. *14* for details.

[b] Ratio for the +1 and +2 oxidation states.

[c] Ratio for the +2 and +3 oxidation states.

[d] With the VSB potential (see text) J is 654 and B is $-795\ cm^{-1}$.

[e] With the VSB potential, J is 459 and B is $-774\ cm^{-1}$.

sponding broken symmetry picture. The broken symmetry state is assumed to exhibit complete trapping, whereas the high-spin state has an $E(S_{max})_u - E(S_{max})_g = 10B$ splitting. The latter splitting is, in fact, similar to the orbital splitting between the lowest unoccupied $a_g\beta$ and $b_{1u}\beta$ seen in Fig. 3. The J_{red} value is determined from the equation,

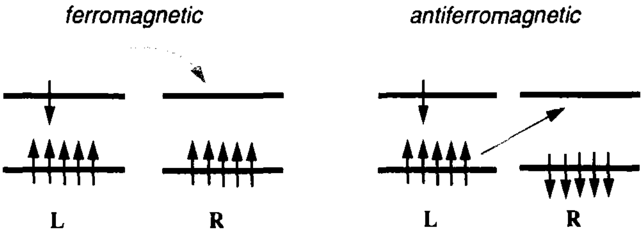

FIG. 4. Delocalization of the added electron in the reduced dimer is compared for the ferromagnetic (F) and antiferromagnetic (AF) configurations. There is loss of spin polarization energy for AF but no loss for F. See Ref. *13*.

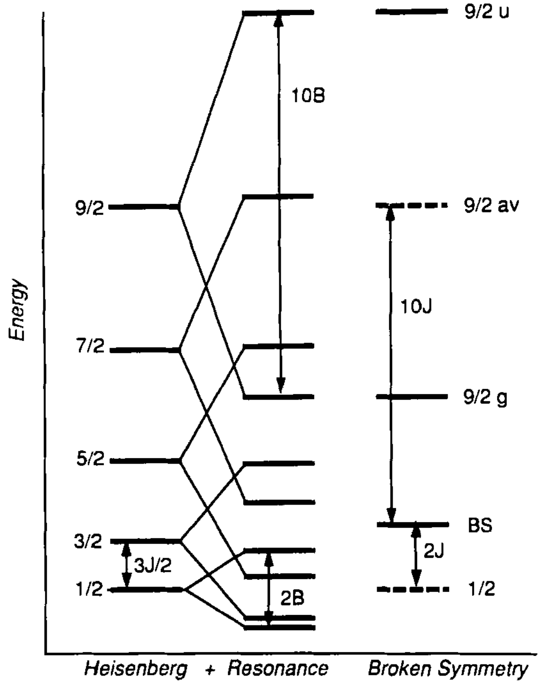

FIG. 5. Schematic spin state diagram for a reduced $Fe_2S_2^{1+}$ dimer. The spin states for a Heisenberg, Heisenberg plus resonance ladder, and within the broken symmetry picture are indicated, including the broken symmetry (BS), and high-spin $S = \frac{9}{2}$ states. $E(S = \frac{9}{2})_{av}$ is taken as the simple average of the $E(S = \frac{9}{2})_{g,u}$ states. See text and Ref. *13*.

$E(S_{max})_{av} - E_B = n(n - 1)J/2 = 10J$ [Eq. (26)], where $E(S_{max})_{av}$ is the average taken over the g, u energies.

The assumption of complete trapping implies that $E(S_{max})_{av}$ can be taken as a simple average of $E(S_{max})_g$ and $E(S_{max})_u$. This should be a fairly good assumption, but it is not exact. An argument can be made with reference to Figs. 1 and 4. In the state $\Psi_L(B)$—where an electron has been added to $16a_1\beta$, Fe $d_{z^2}\beta$ localized on the left—this electron cannot delocalize, since the corresponding orbital of the same spin $10a_1\beta$, Fe $d_{z^2}\beta$ on the right is already occupied. Only a small amount of delocalization of $10a_1\alpha$ (left) to the right side is allowed with molecular orbital (MO) mixing coefficient c, because spin polarization energy is lost on L → R electron transfer (see Fig. 4). Further, only the resonance part of this, giving a further factor $1/\sqrt{5}$, leads to nonorthogonality between $\Psi_L(S)$ and $\Psi_R(S)$ for $S = S_{max}$, where $\Psi_L(S)$ and $\Psi_R(S)$ are obtained by projection from $\Psi_L(B)$ and $\Psi_R(B)$. It is this nonorthogonality that leads to the more general weighted average equation in Ref. *13* in place of the simple average $E(S_{\mathrm{max}})_{\mathrm{av}}$. In the present context, the simple average is well justified. [The proper coefficient for use in Eq. (7) of Ref. *13* is $c' = c/\sqrt{5}$, not c, so that $c' = 0.2$; moreover, c is difficult to calculate accurately.]

The calculated values for the J and B parameters are $J_{\mathrm{red}} = 346\ \mathrm{cm}^{-1}$ and $|B| = 516\ \mathrm{cm}^{-1}$; the ratio $|B|/J_{\mathrm{red}}$ is 1.49 (Table I). Experimental J_{red} values are $196\ \mathrm{cm}^{-1}$ from blue-green algal ferredoxin (*80*) and $220\ \mathrm{cm}^{-1}$ from spinach ferredoxin (*81*); these are all AF. As in the oxidized case, the theoretical prediction overestimates the J value. However, the reduced case is complicated by the presence of the B parameter, which does not appear at all in the Heisenberg Hamiltonian that was used in fitting the magnetic susceptibility data to the Heisenberg model to extract an "experimental J_{red}" value. If we take the Heisenberg plus resonance Hamiltonian seriously, we see that when B is substantial the higher spin states are closer to $S = \frac{1}{2}$ than for the corresponding Heisenberg Hamiltonian. In fact, a higher spin state can become the ground state for large enough B. By plotting the energy versus $|B|/J$, as in the work of Münck *et al.* (*17*), the $S = \frac{3}{2}$ becomes the ground state in place of $S = \frac{1}{2}$ for $1.5 \leq |B|/J \leq 2.5$, whereas for $|B|/J \geq 4.5$ the ground spin state is $S = \frac{9}{2}$. Our calculated $|B|/J_{\mathrm{red}}$ value of 1.49 is nearly at the $S = \frac{1}{2}$, $S = \frac{3}{2}$ crossover point. If, however, a difference in the site energies of the left and right sites is introduced, a new situation is obtained. The higher spin states are less stabilized than with the Heisenberg plus resonance Hamiltonian. When the site energy difference is large, $|E_{\mathrm{L}} - E_{\mathrm{R}}| \gg |B|(S + \frac{1}{2})$, then the resonance term and the site energy difference together combine to give an effective J parameter, $J_{\mathrm{eff}} = J - 2B^2/|E_{\mathrm{L}} - E_{\mathrm{R}}|$ (*17*). The resonance term in the presence of different site energies thus makes an effective ferromagnetic contribution to J_{eff}. Something like this must be happening in reduced 2Fe–2S proteins and clusters. Mössbauer spectroscopy clearly indicates trapped valence. With B of the order of $500\ \mathrm{cm}^{-1}$, the site energy difference (or other mechanisms, such as vibronic coupling) should be sufficient to localize the $S = \frac{1}{2}$ ground state as originally proposed in our 1984 paper. However, there is no simple way to evaluate the separate terms in J_{eff} either theoretically or experimentally. The localization is that of a Robin–Day Class II complex (*82*). Direct evaluation of the B parameter by experimental methods would be quite difficult here; as we discuss below, the situation is more promising in polynuclear Fe–S systems where some dimer subunits have a large net spin.

E. ELECTRON TRANSFER AND OPTICAL CHARGE TRANSFER SPECTRA

The presence of the "inverted level scheme" with S,S*(3*p*) orbitals lying just below empty minority spin Fe(3*d*) levels immediately suggests a role for S(3*p*) in mediating the rapid electron transfer observed between ferredoxins and other redox centers (*13*). We will consider direct transfer of an electron from a negatively charged donor to ferredoxin. Dipole and spin-allowed charge transfer bands (and also spin-forbidden charge transfer bands) of S,S*(3*p*) → Fe(3*d*) appear at low energy in 2Fe–2S proteins (*83–85*). Since these are at low energy (10,000 to 25,000 cm^{-1}), charge transfer intermediate states with a hole in the S(3*p*) band and internal electron transfer cysteine S → Fe d_{z^2} are very likely, the charge transfer (CT) being induced by polarization due to the electric field of the donor. These intermediates are closely analogous to the spin- and dipole-allowed CT excitations. (Whether these are real intermediates or virtual intermediates, essentially quantum mechanical resonances, is an interesting open question.) The electron from the donor can then fill the empty S(3*p*) hole, completing the electron transfer. This mechanism clearly shows how reduction at Fe can occur without direct contact of the Fe center with the donor. Rapid, nearly diffusion-controlled electron transfer of aquated electrons to oxidized $Fe_2S_2^{2+}$ parsley ferredoxin has been measured with a second-order rate constant $k_2 = 9.7 \times 10^9\ M^{-1}\ \mathrm{sec}^{-1}$ (*86*). Electron transfer is also rapid between rubredoxin molecules, with an apparent self-exchange rate constant of 1.7×10^8 to $1 \times 10^9\ M^{-1}\ \mathrm{sec}^{-1}$ (*87*).

VI. Three-Iron Clusters

A. BACKGROUND

The extension of the ideas discussed above to three-iron clusters was pioneered by Münck, Huynh, Girerd, and their co-workers (*17, 33, 88*). Here we can consider both the total spin S and a "subdimer spin" S'. The initial motivation came from analysis of the reduced three-iron cluster in *Desulfovibrio gigas* ferredoxin, which showed clearly that one component of this cluster was a delocalized Fe(II)/Fe(III) dimer with $S' = \frac{9}{2}$ (*33*). Later studies have confirmed that a spin Hamiltonian that contains both Heisenberg and resonance delocalization terms can explain many of the properties in a variety of clusters (*89*). Here we outline the way in which a very simple theory of reduced three-iron clusters can be constructed; the oxidized (all Fe^{3+}) clusters are also of interest, and for our theoretical work on this problem, see Ref. *90*.

B. BROKEN SYMMETRY ANALYSIS OF REDUCED THREE-IRON CLUSTERS

Following the results found for two-iron clusters, we assume that the true electrostatic interactions that couple iron spins together can be replaced by an interaction of the Heisenberg type (*90, 91*):

$$\hat{H} = J(\mathbf{S}_1 \cdot \mathbf{S}_2 + \mathbf{S}_1 \cdot \mathbf{S}_3 + \mathbf{S}_2 \cdot \mathbf{S}_3) \tag{51}$$

and that the off-diagonal matrix elements connecting states where electron delocalization is "allowed" will be of the form $B(S' + \frac{1}{2})$, as discussed above. Consider first a three-iron cluster with three equivalent metal sites in the "singly reduced" Fe(II)/Fe(III)/Fe(III) formal oxidation state. In the high-spin configurations, the first five d electrons on each site are aligned in a parallel fashion, say spin-up. We can form three basis configurations by allowing the final d electron (which must be spin-down) to reside, in turn, on each of the three sites. Using the results cited above, the spin Hamiltonian matrix becomes

$$\mathbf{H}_{\text{hs}} = \begin{bmatrix} (\frac{65}{4})J & 5B' & 5B' \\ 5B' & (\frac{65}{4})J & 5B' \\ 5B' & 5B' & (\frac{65}{4})J \end{bmatrix} \tag{52}$$

Here and below, the diagonal elements represent the system energy in the absence of delocalization, and the off-diagonal elements give the specific resonance delocalization effects, recognizing that $(S' + 1/2) = 5$ for parallel-spin Fe(II)/Fe(III) dimers. The eigenvalues are $E_1 = (\frac{65}{4})J + 10B'$, and $E_{2,3} = (\frac{65}{4})J - 5B'$ (doubly degenerate). For these clusters we find $B' < 0$, and hence E_1 lies lowest.

For the broken symmetry state, the first five d electrons of one of the iron atoms (which we call "*a*") is of spin opposite to that of an equivalent pair "*b*." There are still three basis configurations, corresponding to the three possible locations of the last d electron. Following Papaefthymiou *et al.* (*33*), we will adopt the simplest delocalization hypothesis, that resonance interaction is important only between the two irons of the same spin, pair "*b*." Here the spin matrix is

$$\mathbf{H}_{\text{bs}} = \begin{bmatrix} -(\frac{25}{4})J & 0 & 5B \\ 0 & -(\frac{15}{4})J & 0 \\ 5B & 0 & -(\frac{25}{4})J \end{bmatrix} \tag{53}$$

Here we have allowed the delocalization parameter in the broken symmetry state, B, to differ from that in the high-spin state; the Xα results reported below show that this indeed happens. Eigenvalues for the broken symmetry case are $E_{1,2} = -(\frac{25}{4})J \pm 5B$ and $E_3 = -(\frac{15}{4})J$.

The J and B values can thus be estimated by comparing the energy differences arising from these formulas with those computed from a broken symmetry molecular orbital approach, and estimates of the pure spin state energies (including the ground state energy and its spin value) are then made from the resulting parametrized spin Hamiltonian.

To apply these ideas, we have carried out scattered-wave calculations on models for Fe_3 and $ZnFe_3$ clusters, using the Xα approximation for exchange and correlation effects (*90–92*). Structures of "cubane" 3Fe clusters are not known from high-resolution X-ray crystallography, and our assumptions about the structures are given elsewhere. For the singly reduced 3Fe cluster, a high-spin unrestricted self-consistent wavefunction (with 15 spin-up d electrons and one spin-down d electron) was determined. Then, the spin-up and spin-down potentials of one iron atom were interchanged, and the solution reconverged to a broken symmetry state with a large spin-up spin population on two irons and a large spin-down population on the third. As with the 2Fe clusters, significant spin populations are also found on sulfur centers. The highest occupied orbitals (except for the last one) are primarily of sulfur p character, and the majority-spin Fe d orbitals are below these. For each wavefunction, the very highest occupied orbital is primarily of minority-spin Fe d character. For the high-spin case, the two potential orbitals for this last electron (of a_1 and e symmetry) lead to total energies that are separated by 450 cm^{-1}, which can be identified with $15B'$ through Eq. (52). Hence the effective resonance interaction B' is fairly small, about -30 cm^{-1}. In the broken symmetry case, where delocalization can occur over only two centers (the "b" pair, which have the same spin alignment), we find g and u states (of a' and a'' symmetry) that are split by a much larger amount, 4060 cm^{-1} [which by Eq. (53) is $10B$], so that B is -406 cm^{-1}. The J value for this complex is determined primarily by the difference in the high-spin and broken symmetry energies; fitting the Xα energies to the eigenvalues given above yields $J = 297$ cm^{-1}.

Table I summarizes the results of our calculations, along with previous work on two- and three-iron clusters. As before, the general tendency of the Xα scattered-wave method is to overestimate J: for example, the experimental estimate of J for the oxidized linear three-iron cluster is 300 cm^{-1}, about 45% lower than the value we estimate.

Several interesting features emerge from Table I. First, the magnitude of J decreases as the complexes are reduced. This happens even when the geometries are unchanged, as we have assumed here. It is likely that reduction of the complexes will in addition lead to slight expansions of the core, which would reinforce this drop in J as the complexes are reduced. The magnitudes of J appear to be correlated with geometry: the linear two- and three-iron complexes (with nearly identical bridging geometries) have higher values for J than do the cubanelike clusters. Second, the resonance parameters B are negative, indicating that the symmetric combination of atomic orbitals on the "*b*" irons lies below the antisymmetric combination. As with J, the magnitudes of B appear to be related to the geometry of the bridge, with larger absolute values for the linear than for the cubane geometry. Computed magnitudes of $|B|/J$ are around 1.5; since, however, we expect the computed J values to be too large, we likewise expect the true values of $|B|/J$ to be larger than those shown in Table I, probably in the range 2.0–3.0. For the cubanelike three-iron cluster, with all J values equal, the ground state is predicted to be $S = 2$ (as is observed) when $|B|/J > 2.0$ (*17, 33*).

VII. Four-Iron Clusters

A. ENERGY LEVEL STRUCTURE

4Fe–4S clusters commonly appear in three oxidation states (*93*). All the calculations we will describe are on the model system $[Fe_4S_4(SCH_3)_4]^{1-/2-/3-}$, with the equivalent cubane core oxidation states, $[Fe_4S_4]^{3+/2+/1+}$ (*14, 94, 95*). The calculations have typically been made with an assumed D_{2d} molecular geometry, and with the reduced electronic symmetry of C_{2v} after symmetry breaking. For details about the molecular geometries employed, and computational methodology, we refer to our published work (*14, 94, 95*).

Our basic reference point is the electronic structure of the $[Fe_4S_4]^{2+}$ cluster. In the broken C_{2v} electronic symmetry, the equivalence between the top and bottom halves of the cluster is removed and a spin-polarized calculation is done to determine Ψ_B. Qualitatively, the broken symmetry state is constructed by antiparallel alignment of the two $[Fe_2S_2]^{1+}$ subunits. Each subunit is high spin, so that $S_{12} = S_{34} = \frac{9}{2}$ aligned to give $M_S = 0$, where S_{12}, S_{34} are spin quantum numbers for the dimeric subunits, and M_S is the z component of total cluster spin S. The true spin ground state has both $S = 0$, and $M_S = 0$, and has an energy $E(S = 0)$ below E_B. In Ψ_B each dimeric subunit has 10 occupied majority-spin [mainly Fe(3*d*)] levels at low energy, and one occupied minority-spin Fe(3*d*) level at much higher energy. Between the two exchange-split Fe(3*d*) sets lies the S*(3*p*) and S(3*p*) bands, in accordance with the inverted level scheme. The formal metal oxidation state is $Fe^{2.5+}$, with a formal spin population of 4.5 per iron. Iron sulfur covalency leads to a much lower Fe charge, a smaller Fe spin population, and a higher total Fe *d* population than for these "formal" values.

The highest occupied molecular orbital (HOMO) $20a_1$ is a delocalized Fe–Fe σ bonding orbital $(d_{x^2-y^2})_a + (d_{x^2-y^2})_b$, largely confined to one dimeric subunit of the cluster (Plate 1). It is also weakly Fe–S antibonding (or possibly nonbonding), based on Plate 1. The minority-spin energy levels and various spectroscopic parameters are indicated in Fig. 6 (*94*). Of primary importance is $10B_\sigma$, which gives the splitting between the occupied Fe–Fe σ bonding orbital, $20a_1$, and the empty Fe–Fe σ^* antibonding orbital, $14b_2$. The J parameter is determined from the configuration energy difference between the high-spin state, $E(S_{\max})$ (all spin vectors aligned with $S_{12} = S_{34} = \frac{9}{2}$, $S_{\max} = 9$), and the broken symmetry energy E_B as

$$E(S_{\max}) - E_B = S^2_{\max}J/2 = (n - 1)^2J/2 = 81J/2 \qquad (54)$$

The corresponding pure spin state energy separation for the highest and lowest states of the ladder is

$$E(S_{\max}) - E(S = 0) = S_{\max}(S_{\max} + 1)J/2 = 45J \qquad (55)$$

so $E(S = 0)$ lies $9J/2$ below E_B.

B. OXIDIZED AND REDUCED CONFIGURATIONS

The ligand field levels $20a_1$, $9a_2$, and $14b_2$ (see Fig. 6) (*94*) are also the levels filled or emptied by $Fe_4S_4{}^{2+/1+}$ and $Fe_4S_4{}^{2+/3+}$ redox processes (*14, 95*). In the oxidized (+3) high-potential cluster (HP_{ox}), one of two $20a_1$ electrons is removed. In the reduced (+1) oxidation state, one electron is added either to Fe–Fe σ^* or δ^* so that the final orbital configuration (OC) is OC1 = $(20a_1\alpha, 20a_1\beta, 14b_2\alpha)$ or OC2 = $(20a_1\alpha, 20a_1\beta, 9a_2\alpha)$ (*14, 96*). These are nearly degenerate in energy, with OC2 slightly lower by about 0.1 eV (*14, 95*). Since the cluster geometry D_{2d} is rather idealized, and the cluster geometry and environment may provide distortions or asymmetries, we can expect a mixing and splitting of the two orbital configurations OC1 and OC2. The variability of the quadrupole splittings on the $2Fe^{2+}$ pair among different $Fe_4S_4{}^{1+}$ clusters and proteins is consistent with the large difference in the

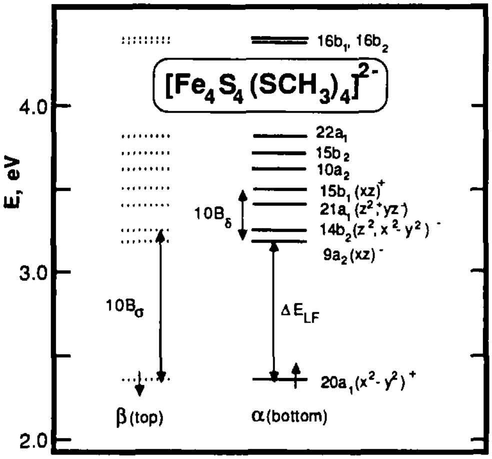

FIG. 6. Xα–LCAO energies for the ligand field levels (highest occupied and lowest unoccupied levels) of $[Fe_4S_4(SCH_3)_4]^{2-}$. All these levels are mainly Fe(3*d*). Spin α and β levels are specified with solid and dotted lines, and their location on the top and bottom faces of the cluster is indicated. See Ref. *94*.

calculated ΔE_Q on the $2Fe^{2+}$ reduced sites (*14, 96*). Further, the presence of these two nearly degenerate configurations, OC1 and OC2, is relevant to the relative stability of an $S = \frac{1}{2}$ versus $S = \frac{3}{2}$ ground state.

C. RELAXATION EFFECTS ON CLUSTER OXIDATION +2 → +3

Plates 1 and 2 show the orbital amplitude in orbital $20a_1\alpha$ of the +2 cluster, and the total valence electron density difference between the reduced (+2) and oxidized (+3) states, respectively. Both calculations used the same (+2) geometry, so the differences are entirely electronic and contain no effects from geometry changes on oxidation (in contrast to experimental X-ray density difference maps, which give a composite of electronic and geometric effects) (*93*). (Further, the isovalue contour levels for the orbital map were set to the plus/minus square roots, gray/blue, of the positive contour level for the density difference map, so these are strictly comparable; isovalues for Plates 3 and 4 were set to the same values as for Plates 1 and 2, respectively.) The blue region on Plate 2 is the region of net electron depletion on oxidation, mainly on the two oxidized irons and on all sulfurs, and the green region shows the backflow of electron density, giving a compensating region of increased electron density. The blue region in Plate 2 resembles the $20a_1$ orbital

(Plate 1) around the oxidized iron centers, as one might expect. However, there are two major differences between the orbital density and the total electron density difference. First, the charge depletion region on Plate 2 is much larger and more diffuse than in the orbital map; it extends to all terminal and bridge sulfurs, and shows that the charge on sulfurs becomes considerably less negative on oxidation. Second, the backflow of electron density, which represents bonding density and $S \rightarrow$ Fe electron donation, is completely absent in the orbital map (Plate 1). Both of these effects are consequences of electron relaxation in the "passive" orbitals (all orbitals except $20a_1\alpha$).

Some physically important consequences follow from this electron density difference map: (1) the cluster oxidation is an electronically asymmetric process; (2) since the charge depletion occurs from the weakly Fe–S antibonding orbital $20a_1\alpha$, and backflow arises from bonding density via S → Fe electron donation to the $2Fe^{3+}$ oxidized centers, there should be asymmetric Fe–S bond strengthening confined largely to the "oxidized" layer of the cluster; (3) all sulfur centers become less negative on oxidation by about 0.1 electron per sulfur; (4) the net Fe(3*d*) population decreases by only 0.05–0.07 electron per iron for the oxidized iron sites, but there is considerable charge rearrangement on these sites.

The electron density difference map lends further support to the analysis we have given of resonance Raman spectra for *Chromatium vinosum* $Fe_4S_4^{2+/3+}$ and $Fe_4Se_4^{2+/3+}$ high-potential proteins (*97*). The observed increase in Fe–S terminal stretch frequencies and the lower symmetry of the vibrations in the oxidized (+3) compared with the reduced (+2) form correspond to points 1 and 2 above. Higher Fe–S* stretch frequencies are not observed, although these are also implicated by our calculations. Both Fe–S terminal and Fe–S* bond strengthening on oxidation is also implied by the shorter Fe–S* and Fe–S terminal bond lengths as seen in the structure of a synthetic $Fe_4S_4^{3+}$ cluster, by about 0.02 and 0.04 Å, respectively, compared with synthetic +2 clusters (*98*). Longer NH–S hydrogen bonds (by about 0.1–0.4 Å) to many of the S_t, S* atoms have been found from the protein X-ray structure of

---

PLATE. 1. Orbital $20a_1\alpha$ (+2) form of 4Fe–4S cluster, showing atoms of Fe (purple), S (yellow), C (green), and H (small, light-blue spheres). Positive/negative amplitudes are gray/blue, and isovalue levels are set as the plus/minus square roots of those in Plate 2. The top layer on all plates corresponds to the bottom layer in Fig. 6.

PLATE. 2. Total valence electron density difference +2 − +3. Blue shows net electron depletion on oxidation and green shows increased density.

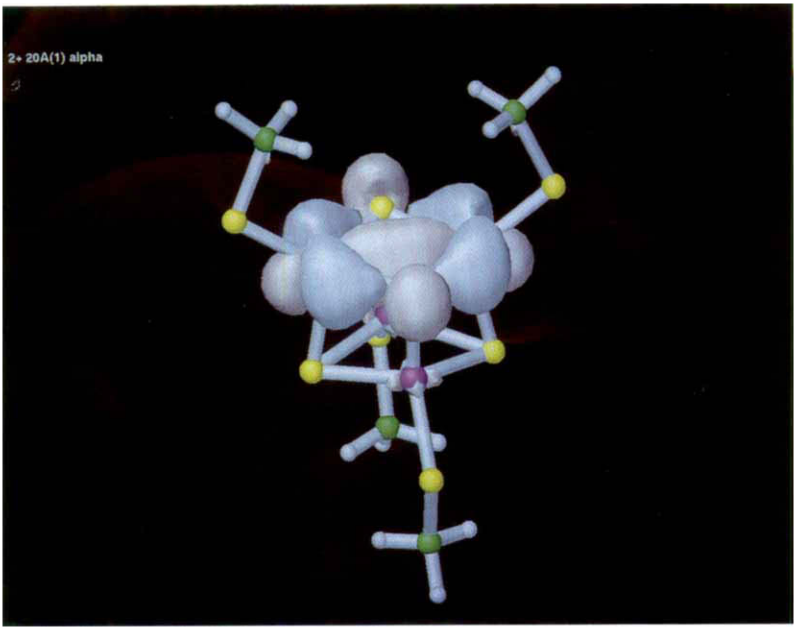

PLATE 1.

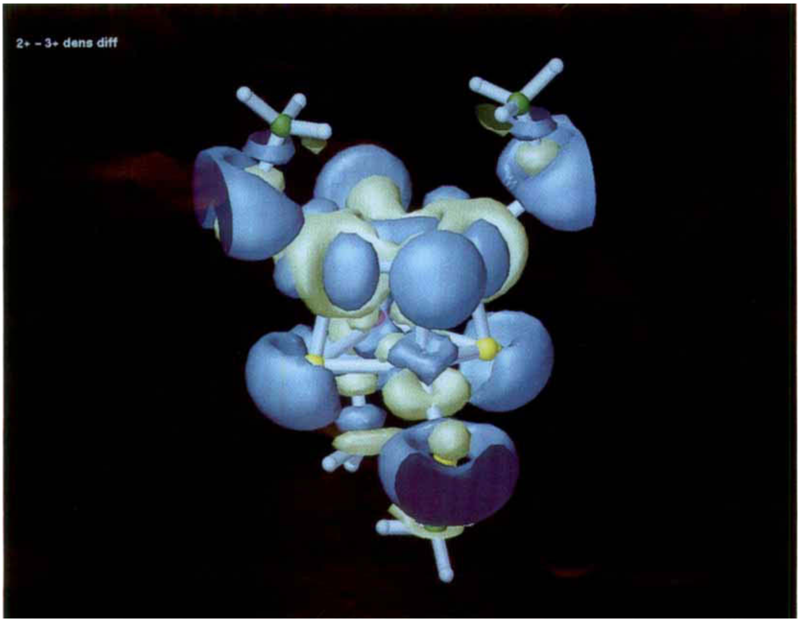

PLATE 2.

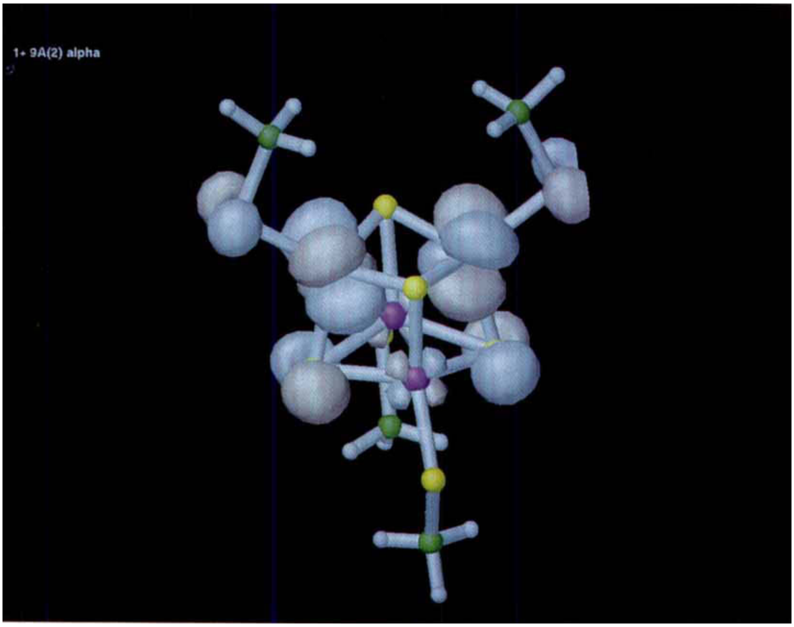

PLATE 3.

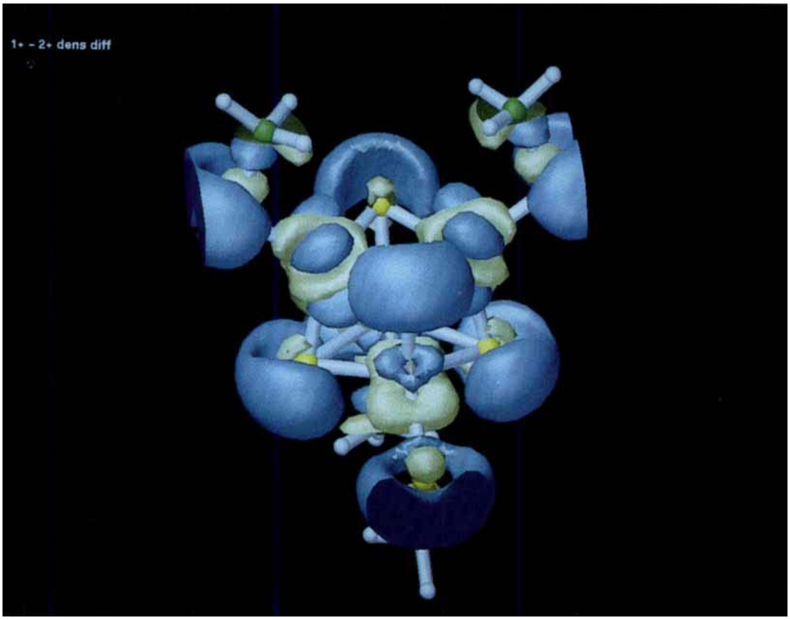

PLATE 4.

HP_{ox} compared to the reduced protein or to ferredoxins (*93*). These are consistent with the less negative charge on all S, S* in the oxidized form (point 3). The changes in electron density on oxidation are quite spread out, and modeling of redox effects on hydrogen bond strengths should take this into account. For example, the increase in hydrogen bond strength for (reduced minus oxidized) high-potential iron protein (HiPIP) is probably considerably less for each H bond than in the local model of Sheridan *et al.*, but most or all H bonds would be strengthened (*99*).

The modest difference in Mössbauer isomer shift observed when comparing the Fe_{ox} sites of +3 synthetic clusters and proteins to Fe sites in +2 clusters (*100*) is consistent with the small change calculated in net $Fe(3d)_{ox}$ population on oxidation (point 4).

D. RELAXATION EFFECTS ON CLUSTER REDUCTION $+2 \rightarrow +1$

Plate 3 shows the highest orbital of $Fe_4S_4^{1+}$, which resides largely on the reduced half of the cluster, $9a_2\alpha$ (HOMO) in configuration OC2. Again the total valence electron density difference (Plate 4) for +1 minus +2 includes substantial relaxation effects, and therefore differs from the HOMO $9a_2\alpha$. On Plate 4, blue represents increased electron density and yellow represents decreased density upon reduction. The net Fe(3*d*) population on the reduced iron sites increases by only about 0.05–0.10 electron per iron on reduction, whereas all sulfur populations increase by about 0.1 per sulfur (with more than 0.8 electron going to all eight sulfurs). Sulfur as well as iron is thus involved in the changes in electron distribution on reduction.

E. SPIN-COUPLING PARAMETERS

Our spin Hamiltonian model for 4Fe clusters closely follows the ideas outlined above for smaller systems. The proposed spin Hamiltonian solution for the pure spin states of the +2 form is

$$E(S) = (J/2)S(S+1) \pm B(S_{34} + \tfrac{1}{2}) \pm B(S_{12} + \tfrac{1}{2}) \qquad (56)$$

PLATE. 3. Orbital $9a_2\alpha$ (+1) form of cluster. Labeling and isovalues as in Plate 1.

PLATE. 4. Total valence electron density difference +1 − +2. Blue shows increased electron density on reduction and green shows decreased density. Same isovalues as in Plate 2.

with S_{12} and S_{34} as the spin quantum numbers for the two mixed-valence pairs. Energies for the +1 and +3 states are

$$E(S) = (J/2)S(S+1) \pm B(S_{34} + \tfrac{1}{2}) \pm B'(S + \tfrac{1}{2}) + C_1 \tag{57}$$

where for +3, S_{12} is the spin quantum number for the $2Fe^{3+}$ pair, and for +1, S_{12} is the spin for $2Fe^{2+}$. For all three oxidation states, S_{34} is the spin of the Fe^{2+}–Fe^{3+}, and S is the total spin quantum number. The first term in Eq. (57) is the Heisenberg coupling energy, the second is the resonance delocalization energy of the mixed-valence pair with parameter B, and the third represents the possibility of resonance of sites 1, 2 with 3, 4 ("interlayer resonance") involving the parameter B'. The last term is a spin-independent constant (C_1).

We will focus on the +1 cluster form, seeking the broken symmetry and high-spin energy equations necessary to determine the coupling parameters. The broken symmetry energy equation is

$$\begin{aligned} E_B &= J\langle \mathbf{S}_{12} \cdot \mathbf{S}_{34} \rangle \pm B(S_{34} + 1/2) + C_2 \\ &= -J(n-1)(n-2)/4 \pm 10B + C_2 = -18J \pm 10B + C_2 \end{aligned} \tag{58}$$

where

$$C_2 = J\langle \mathbf{S}_1 \cdot \mathbf{S}_2 \rangle + J\langle \mathbf{S}_3 \cdot \mathbf{S}_4 \rangle$$

with $n - 2 = 8$ being the maximum number of unpaired electrons for $2Fe^{2+}$. Here C_2 is a constant for fixed quantum numbers S_{12} and S_{34}. The corresponding equation for the energies of the high-spin states is

$$\begin{aligned} E(S_{\max}) &= J\langle \mathbf{S}_{12} \cdot \mathbf{S}_{34} \rangle \pm B(S_{34} + \tfrac{1}{2}) \pm B'(S + \tfrac{1}{2}) + C_2 \\ &= +J(n-1)(n-2)/4 \pm 10B \pm B'(S + \tfrac{1}{2}) + C_2 \\ &= +18J \pm 10B \pm 9B' + C_2 \end{aligned} \tag{59}$$

with $S_{\max} = \frac{17}{2}$ for the +1 cluster. Equations (58) and (59) are sufficient to determine the J, B, and B' parameters from the density-functional energies. J is determined from the configuration energy difference between the high-spin and the broken symmetry SCF energies, while B and B' were determined from orbital energy differences. The parameters for the oxidized (+3) state are determined in a similar fashion.

Table I collects results for a number of our calculations (*13, 14, 91, 92, 94, 95*). The density-functional LCAO results for the $Fe_4S_4^{1+/3+}$ clusters have not been published previously; corresponding LCAO results for the +2 cluster are from Ref. *94*. The general trend that $J_{ox} > J_{red}$ is seen in the comparison of 2Fe–2S, 3Fe–4S, and 4Fe–4S cluster oxidation states by either Xα–SW or Xα–LCAO (also VSB potential).

[The VSB potential is a local spin density (LSD) potential due to Vosko *et al.* with a correlation correction due to Stoll *et al.* and an exchange energy gradient term due to Becke] (*57–61*). Geometry A is based on the experimental synthetic model geometry for +2 clusters whereas geometry B is a typical expanded geometry for the +1 cluster. The interlayer resonance parameter is seen to be significant in the sense that the three-parameter model parameters differ from the two-parameter fits (J and B), where B' is ignored. This is particularly strong for the +1 state (OC2) and where the cluster is expanded so that the B'/J is larger.

A summary of spectroscopic and spin-coupling parameters for $[Fe_4S_4]^{2+}$ is given in Table II, which also compares values from Xα–LCAO and Xα–SW (*94*). The two methods give parameters that are quite close. For the J parameter, Holm's group has obtained values of about 450–550 cm^{-1} from magnetic susceptibility fits for an analogous synthetic cluster, which is rather close to our calculated values (*101*). However, a combined Heisenberg plus resonance Hamiltonian would give both J and B parameters from fits to Eq. (56), and J would be expected to change significantly from the fit using a Heisenberg Hamiltonian alone. Two other points are of significance. The resonance B_σ pathway is clearly much stronger than the B_δ pathway within each resonance pair. The ligand field splitting between $20a_1$ and $9a_2$ is fairly large, with a substantial contribution from the stronger B_σ than B_δ resonance (see also Fig. 6). Qualitatively, the low-lying character of $20a_1$ compared to the other ligand field levels makes an electronic contribution to the high positive redox potential of the HP cluster +2/+3 redox process. A more quantitative assessment requires a consideration of solvation and other effects.

TABLE II

SPECTROSCOPIC AND SPIN-COUPLING PARAMETERS FOR $[Fe_4S_4(SCH_3)_4]^{2-}$[a]

Parameter	Xα–LCAO	Xα–SW
J	454	401
B_σ	−740	−585
B_δ	248	239
ΔE_{LF}	6751	5243

[a] Values in cm^{-1}. See Fig. 6 and the text for definitions of the parameters. See Ref. *94*.

F. STABILITY OF $S = \frac{1}{2}$ VERSUS $S = \frac{3}{2}$ FOR REDUCED (+1) CLUSTERS

The experimental observation of a variety of spin ground states, $S = \frac{1}{2}$, $\frac{3}{2}$, or $\frac{7}{2}$, in reduced $Fe_4S_4^{1+}$ and $Fe_4Se_4^{1+}$ clusters and proteins, is an important discovery by a number of groups (*102–107*). From a theoretical perspective [see Blondin and Girerd (*18*) and Borshch and Chibotaru (*108*)] interlayer resonance has been considered as a mechanism of possible significance for spin equilibria in both $Fe_3S_4^0$ cubane and in $Fe_4S_4^{3+/1+}$ clusters. The question is where and under what circumstances this mechanism will alter the spin ground state, or the low-lying excited spin states. Our very recent Xα–LCAO calculations cast some light on this problem. For the +1 cluster, Table I gives $J = 300\ \text{cm}^{-1}$, $|B'| = 622\ \text{cm}^{-1}$ with a ratio $|B'|/J = 2.1$ for the expanded geometry B of OC2, for which Eq. (57) yields an $S = \frac{3}{2}$ ground state with low-lying $S = \frac{5}{2}$ and $S = \frac{1}{2}$ excited states. The situation of interlayer resonance in reduced $Fe_4S_4^{1+}$ clusters bears a close analogy to the resonance problem in reduced $Fe_2S_2^{1+}$ [compare Eqs. (50) and (57); see also Münck *et al.* (*17*)]. By contrast to OC2 (which has δ^* interlayer resonance), the orbital configuration OC1 (with σ^* interlayer resonance) should have $B' = 0$ by symmetry, which gives an $S = \frac{1}{2}$ ground state. Of course, the D_{2d} geometric symmetry is not exact, and mixing and splitting of OC1 and OC2 are to be expected. We note as well that the $2Fe^{2+}$ reduced pair Mössbauer ΔE_Q is always considerably smaller experimentally in $S = \frac{3}{2}$ ground state clusters than in $S = \frac{1}{2}$ type clusters (*102–107*), consistent with the lower calculated ΔE_Q for OC2 than for OC1 (*14, 96*). This is true whether or not all 4Fe sites have the same ΔE_Q. This explanation for the presence of an $S = \frac{3}{2}$ ground state in some clusters is physically distinct from the one proposed in our recent phenomenology papers, based on an inequality between $J(Fe^{2+}–Fe^{2+})$ and $J(Fe^{3+}–Fe^{2+})$ (*96, 109*). Though both mechanisms may be present, the interlayer resonance mechanism appears to be more robust in yielding an $S = \frac{3}{2}$ ground state. The competition between the Heisenberg term and the B' term is rather delicate, yielding a stabilization of about 170 cm^{-1} for $S = \frac{3}{2}$ compared to $S = \frac{1}{2}$ in the absence of any localizing forces. A more detailed analysis of this problem will be presented elsewhere.

G. PHENOMENOLOGICAL MODELING OF OXIDIZED (+3) AND REDUCED (+1) CLUSTERS

We have previously noted the trend in Heisenberg coupling constants, $J(2Fe^{2+}) < J(Fe^{2+}–Fe^{3+}) < J(2Fe^{3+})$, which is verified both from our calculations on 2Fe, 3Fe, 3Fe–Zn, and 4Fe complexes (*13, 91, 92, 95*) and from experimental Heisenberg parameters in these systems (*101, 110*). A combined Heisenberg plus resonance Hamiltonian can be constructed with unequal Heisenberg parameters, and having a single resonance interaction within a specific mixed-valence pair. The resonance interaction is of the form $\pm B(S_{34} + \frac{1}{2})$, and neglects any interlayer resonance ($B' = 0$). (We may contrast this with the preceding section, where all J parameters are assumed equal but where $B' \neq 0$.) We have explored the consequences of such phenomenological models for both HP +3 clusters (*111*) and for reduced +1 clusters where the core is $Fe_4Se_4{}^{1+}$ or $Fe_4S_4{}^{1+}$ (*96, 109*). Many important phenomena can be derived from these models, and the appropriate ranges of the Heisenberg parameters plus the resonance parameter can be estimated from our density-functional calculations.

In HP +3 clusters, taking the trend in J values above, and with $B/J > 0.9$, $\Delta J_{12}/J < 0.25$, (*110, 111*), the model gives a ground state of the type $|S_{34}\, S\, S_{12}\rangle = |\frac{9}{2}\, \frac{1}{2}\, 4\rangle$, which with reasonable assumptions about the intrinsic site g_i and hyperfine a_i values (*33*), yields observed effective isotropic hyperfine parameters A_i and average total g value g_{eff} in fairly good agreement with those obtained from magnetic Mössbauer, ENDOR, and EPR spectroscopies (*100, 112*). Here $\Delta J_{12} = J(2\text{Fe}^{3+}) - J$, where $J(2\text{Fe}^{3+})$ is the ferric pair and J (with no subscript) is the interlayer coupling parameter. The latter describes four equal interlayer site couplings (*111, 110*). Phenomenological fits to the magnetic susceptibility for a synthetic HP analog indicate the presence of a very low-lying spin state of the form $|\frac{7}{2}\, \frac{1}{2}\, 3\rangle$ nearly degenerate with the state above, one further low-lying $S = \frac{1}{2}$ state, and two $S = \frac{3}{2}$ states, $|\frac{9}{2}\, \frac{3}{2}\, 3\rangle$ and $|\frac{7}{2}\, \frac{3}{2}\, 2\rangle$ (*110*). Further, the susceptibility fits give an interlayer J coupling of 652 cm^{-1}, $|B| = 529\ \text{cm}^{-1}$, compared with the theoretical values $J = 416\ \text{cm}^{-1}$, $|B| = 722\ \text{cm}^{-1}$ (Table I).

Since the hyperfine and EPR properties of $|\frac{7}{2}\, \frac{1}{2}\, 3\rangle$ are predicted to be very close to those of $|\frac{9}{2}\, \frac{1}{2}\, 4\rangle$, it is difficult to distinguish these states, and either may be the ground state. We have calculated both the **g** tensor and the anisotropic part of the **A** tensors from density-functional methods, and using the vector model based on the Wigner–Eckart theorem. These results will be reported separately. For the present, we give the **g** tensor principal values for the state $|\frac{9}{2}\, \frac{1}{2}\, 4\rangle$ as $g_x = 2.02$, $g_y = 2.02$, and $g_z = 2.07$ in C_{2v} symmetry. Here the z axis is the S_4 axis perpendicular to the Fe^{2+}–Fe^{3+} pair bond x axis, and to the Fe^{3+}–Fe^{3+} pair bond y axis. (The z axis is also the axis of compression for the cluster.) These results are in good agreement with experimental EPR g values on high-potential proteins and synthetic analogs (*100, 112,* *113*). It may be feasible to distinguish between the two possible ground states by ENDOR of the proton hyperfine coupling. (*121, 122*).

For reduced +1 clusters, J values are typically lower than for +2 and +3 clusters, and a substantial inequality between the smaller $J_2(2Fe^{2+})$ and larger $J_1(Fe^{2+}–Fe^{3+})$ parameters is often expected. With three Fe–Fe Heisenberg pairwise couplings of each type and resonance delocalization as well, the modeling requires the use of Racah algebra. The implications of phenomenological models of this type with a single resonance-delocalized pair (with parameter B) have been explored (*96, 109*). In addition to providing a good general account of isotropic hyperfine and g values for various $S = \frac{1}{2}$ states, the model gives a clear analysis of the physical basis for the coexistence of a delocalized $S = \frac{1}{2}$ state and a localized $S = \frac{7}{2}$ state, as found in reduced Se clostridial ferredoxin. The presence of external localizing forces is also quite important in determining the spin ground state and degree of delocalization. Further, there is a simple proposed mechanism for the presence of two states with significantly different rhombic EPR tensors in the unusual cluster in *Desulfovibrio vulgaris* hydrogenase (*114*), provided that the later is, in fact, a reduced 4Fe–4S cluster.

VIII. Conclusions and Prospects for Future Work

A. SUMMARY

A brief summary of some of the important areas wherein theory has made a contribution follows: (1) there is an inverted level scheme in both mononuclear and polynuclear Fe–S complexes with empty Fe(3*d*) levels in close energetic proximity to filled S(3*p*) levels (*14, 64*); (2) spin polarization effects produce both a large intraatomic exchange splitting between majority spin and minority spin Fe(3*d*) levels and significant spin transfer to the ligands (*9, 13*); (3) orbital relaxation effects on oxidation or reduction are large, and implicate both S, S* and Fe in redox processes (*13, 14, 97*); (4) there is a close connection between valence delocalization (resonance delocalization or "double exchange") and spin coupling (*13, 17*); this produces a distinctive term in the spin Hamiltonian; (5) trapped valence in reduced 2Fe–2S systems is produced by competition between resonance and Heisenberg coupling terms in the presence of external localizing forces; by contrast, the pair delocalization observed in 3Fe–4S and 4Fe–4S systems results because some pair spin vectors can be large, facilitating delocalization while maintaining many other pair spin vectors antiparallel, this being related to the concept of "spin frustration" in Hamiltonians having only Heisenberg-type terms (*17, 18*); (6) the general trend $J_{ox} > J_{red}$ is found for most clusters both theoretically and experimentally (*92, 101*); (7) the complex spin state crossovers and equilibria found especially in reduced 4Fe–4S and 4Fe–4Se clusters arise from the interplay of different Heisenberg J parameters with resonance delocalization, and from the presence of localizing forces of various possible types (*96, 109*); resonance may either involve a specific mixed-valence pair, or there may be additional interlayer resonance; (8) density-functional calculations give numerical estimates of J and B parameters, providing a starting point for detailed comparisons with experiment.

In all of these areas, both quantitative density-functional calculations and phenomenological modeling have been valuable. The first is characterized by the ability to make concrete predictions about spectroscopy and energetics for structurally well-defined systems, and by the ability to picture electron densities and spin densities in three-dimensional space. Further, density-functional theory combined with the concept of broken symmetry has a hierarchical conceptual structure, passing from energy levels and orbitals to electron and spin densities. From here, a connection can be made to spin-dependent properties, and the energies of different electron orbital and spin configurations can be related to spin-coupling Hamiltonians and their solutions.

The phenomenological approach has its own advantages, being characterized by flexibility and the possibility for exploration. There is no requirement here for the system to be well-defined geometrically, and even the coordination geometry may not be completely defined (although both are helpful for determining reasonable parameter ranges). Certainly, phenomenological models are the natural meeting place for experiment and theory. Here one optimizes the fit of a chosen model to experimental data (*110*). Our experience in Fe–S systems indicates that a proper "physical" model of a system may require fitting different types of experiments, such as EPR, ENDOR, NMR, Mössbauer, optical, and magnetic susceptibility, to an individual model. For example, infrared measurements provide a potential means of directly determining the B parameter in 4Fe–4S complexes, whereas other measurements are sensitive to both B and J parameters. These results can also serve to exclude physically unacceptable models (*96, 109, 111*).

At present, both the fitting of data to models and quantitative density-functional calculations have been restrictive in the number of J and B parameters determined, but we can look forward to density-functional calculations that will determine unequal J parameters as well as B and B' parameters and to a variety of measurements and fitting procedures that will experimentally determine these same parameters. Further improvements in our theoretical methods are to be expected. At the same time, there appears to be a better correspondence between theoretical and experimental J values in 4Fe than in 2Fe or 3Fe systems. This is possibly due either to the larger high-spin minus broken symmetry energy difference in the 4Fe case [also a larger multiple of J, comparing, for example, $81J/2$ with $25J/2$ from Eqs. (54) and (25)], or due to the more realistic thiolate ligand model used. In many cases, only a lower bound to the J value can be determined experimentally, because susceptibility measurements are only feasible within a limited temperature range (*89*). The experimental determination of B parameters has only begun (*110*). We note here the single case in which B has been measured by UV-visible spectroscopy in an iron–hydroxo dimer complex; this is the first delocalized $S = \frac{9}{2}$ Fe dimer complex ever found (*115*). This optical transition is relatively high in energy ($10B = 13{,}000\ \mathrm{cm}^{-1}$) compared with corresponding transitions predicted theoretically ($10B = 4000\text{–}7000\ \mathrm{cm}^{-1}$) in Fe–S polynuclear complexes, probably because of the short Fe–Fe bond distance (2.5 Å) in the iron–hydroxo dimer system. Of course, there may be more surprises in store in the area of spin coupling and electron delocalization than are presently anticipated.

B. New Directions

There are many important areas for future development. We have begun work on the energetics of cluster bonding, starting with the evaluation of the mean energy of Fe–S bonds in 4Fe–4S clusters (*94*). We have new results on redox potentials for both $+2/+1$ and $+3/+2$ couples of model clusters in the presence of solvent. It will be interesting to extend these results to investigate the effects of protein–cluster interactions on redox potentials, and on the electronic structure of clusters. Protein–cluster interactions can be mediated through hydrogen bonding, longer range electrostatic interactions, and solvation. The effects of asymmetric ligation of the Fe sites (by hydroxyl or carboxylate, for example) should have significant effects on electronic structure (*7*), as will the presence of mixed-metal coordination (Mo, Ni, and Zn) in various enzymes (*17, 116–119*). The electron transfer pathways to and from the cluster should involve electronic polarization, but this is not well understood (*13*). Further, spin coupling and valence delocalization would be expected to play a significant role in tuning the redox potential (*120*), an area that deserves careful investigation. On all of these problems, the interaction of experimental and theoretical approaches seems the best strategy for further advances.

ACKNOWLEDGMENTS

We thank E. Münck, B. H. Huynh, B. Lamotte, E. P. Day, J. M. Moulis, J. Gaillard, J. Jordanov, E. Roth, J. M. Mouesca, G. Rius, D. Stout, G. Blondin, and J. J. Girerd for valuable discussions, and H. Beinert and M. C. Kennedy for their encouragement and insights. We thank E. J. Baerends for the use of the Amsterdam LCAO density functional programs, and P. Vernooijs for technical assistance. We thank M. Pique for his work on the color graphics pictures using the Stardent AVS hardware and software. This work was supported by NIH Grant GM39914.

REFERENCES

1. Ibers, J. A., and Holm, R. H., *Science* **209,** 223 (1980).
2. Beinert, H., *FASEB J.* **4,** 2483 (1990).
3. Burgess, B. K., *in* "Molybdenum Enzymes" (T. G. Spiro, ed.), p. 161. Wiley, New York, 1985.
4. Scott, R. A., Li, P. M., and Chan, S. I., *Ann. N.Y. Acad. Sci.* **550,** 53 (1988).
5. Kim, D. H., Britt, R. D., Klein, M. P., and Sauer, K., *J. Am. Chem. Soc.* **112,** 9389 (1990).
6. Brudvig, G. W., Beck, W. F., and de Paula, J. C., *Annu. Rev. Biophys. Biophys. Chem.* **18,** 25 (1989).
7. Beinert, H., and Kennedy, M. C., *Eur. J. Biochem.* **186,** 5 (1989).
8. Gibson, J. F., Hall, D. O., Thornley, J. H. M., and Whatley, F. R., *Proc. Natl. Acad. Sci. U.S.A.* **56,** 987 (1966).
9. Sands, R. H., and Dunham, W. R., *Q. Rev. Biophys.* **7,** 443 (1975).
10. Norman, J. G., Jr., and Jackels, S. C., *J. Am. Chem. Soc.* **97,** 3833 (1975).
11. Bair, B. A., and Goddard, W. A., *J. Am. Chem. Soc.* **100,** 5669 (1978).
12. Norman, J. G., Jr., Ryan, P. B., and Noodleman, L., *J. Am. Chem. Soc.* **102,** 4279 (1980).
13. Noodleman, L., and Baerends, E. J., *J. Am. Chem. Soc.* **106,** 2316 (1984).
14. Noodleman, L., Norman, J. G., Jr., Osborne, J. H., Aizman, A., and Case, D. A., *J. Am. Chem. Soc.* **107,** 3418 (1985).
15. Noodleman, L., and Norman, J. G., Jr., *J. Chem. Phys.* **70,** 4903 (1979).
16. Ballhausen, C. J., "Molecular Electronic Structures of Transition Metal Complexes." McGraw-Hill, Chatham, U.K., 1979.
17. Münck, E., Papaefthymiou, V., Surerus, K. K., and Girerd, J. J., *in* "Metal Clusters in Proteins" (L. Que, Jr., ed.), ACS Symp. Ser. 372, p. 302. American Chemical Society, Washington, D.C., 1988.
18. Blondin, G., and Girerd, J. J., *Chem. Rev.* **90,** 1359 (1990).
19. Loth, P. de, Cassoux, P., Daudey, J. P., and Malrieu, J. P., *J. Am. Chem. Soc.* **103,** 4007 (1981).
20. Loth, P. de, Karafiloglou, P., Daudey, J. P., and Kahn, O., *J. Am. Chem. Soc.* **110,** 5676 (1988).

21. Astheimer, H., and Haase, W., *J. Chem. Phys.* **85,** 1427 (1986).
22. Kahn, O., *Angew. Chem., Int. Ed. Engl.* **24,** 834 (1985).
23. Yamaguchi, K., Tsunekawa, T., Toyoda, Y., and Fueno, T., *Chem. Phys. Lett.* **143,** 371 (1988).
24. Yamaguchi, K., Fueno, T., Ueyama, N., Nakamura, A., and Ozaki, M., *Chem. Phys. Lett.* **164,** 210 (1989).
25. Hart, J. R., Rappe, A. K., Gorun, S. M., and Upton, T. H., *Inorg. Chem.* (submitted).
26. Hay, P. J., Thibeault, J. C., and Hoffman, R., *J. Am. Chem. Soc.* **97,** 4884 (1975).
27. Anderson, P. W., *in* "Solid State Physics" (D. Turnbull, ed.), p. 99. Academic Press, New York, 1963.
28. Noodleman, L., *J. Chem. Phys.* **74,** 5737 (1981).
29. Noodleman, L., and Davidson, E. R., *Chem. Phys.* **109,** 131 (1986).
30. Anderson, P. W., and Hasegawa, H., *Phys. Rev.* **100,** 675 (1955).
31. Zener, C., *Phys. Rev.* **82,** 403 (1951).
32. Girerd, J. J., *J. Chem. Phys.* **79,** 1766 (1983).
33. Papaefthymiou, V., Girerd, J. J., Moura, I., Moura, J. J. G., and Münck, E., *J. Am. Chem. Soc.* **109,** 4703 (1987).
34. Borshch, S. A., Kotov, I. N., and Bersuker, I. B., *Sov. J. Chem. Phys.* **3,** 1009 (1985).
35. Belinskii, M. I., Tsurkerblat, B. S., and Gerbeleu, N. V., *Sov. Phys.-Solid State (Engl. Transl.)* **26,** 1142 (1983).
36. Karpenko, B. V., *J. Magn. Magnetic Mater.* **3,** 267 (1976).
37. McWeeney, R., and Sutcliffe, B. T., "Methods of Molecular Quantum Mechanics." Academic Press, New York, 1976.
38. Ziegler, T., Rauk, A., and Baerends, E. J., *Theor. Chim. Acta* **43,** 261 (1977).
39. Dunlap, B. I., *Phys. Rev. A* **29,** 2902 (1984).
40. Ross, P., and Solomon, E. I., *J. Am. Chem. Soc.* **113,** 3246 (1991).
41. Bencini, A., *J. Chim. Phys.* **86,** 763 (1989).
42. Albonico, C., and Bencini, A., *Inorg. Chem.* **27,** 1934 (1988).
43. Bencini, A., and Gatteschi, D., *J. Am. Chem. Soc.* **108,** 5763 (1986).
44. Amos, A. T., and Hall, G. G., *Proc. R. Soc. London, Ser. A* **263,** 483 (1961).
45. Martin, R. L., and Davidson, E. R., *Phys. Rev. A* **16,** 1341 (1977).
46. Anderson, P. W., *Phys. Rev.* **115,** 2 (1959).
47. Rose, M. E., "Elementary Theory of Angular Momentum." Wiley, New York, 1957.
48. Heine, V., "Group Theory in Quantum Mechanics." Pergamon, Oxford, 1960.
49. Merzbacher, E., "Quantum Mechanics," 2nd Ed. Wiley, New York, 1970.
50. Lowdin, P. O., *Phys. Rev.* **97,** 1509 (1955).
51. Nesbet, R. K., *Ann. Phys.* **3,** 397 (1958).
52. Nesbet, R. K., *Ann. Phys.* **4,** 87 (1958).
53. Ziegler, T., and Tschinke, V., *in* "Density Functional Methods in Chemistry" (J. K. Labanowski and J. W. Andzelm, eds.), p. 139. Springer-Verlag, New York, 1991.
54. Slater, J. C., *Adv. Quantum Chem.* **6,** 1 (1972).
55. Cook, M., and Karplus, M., *J. Phys. Chem.* **91,** 31 (1987).
56. Case, D. A., *Annu. Rev. Phys. Chem.* **33,** 151 (1982).
57. Vosko, S. H., Wilk, L., and Nusair, M. *Can. J. Phys.* **58,** 1200 (1980).
58. Painter, G. S., *Phys. Rev. B.* **24,** 4264 (1981).
59. Stoll, H., Golka, E., and Preuss, H., *Theor. Chim. Acta* **55,** 29 (1980).
60. Stoll, H., Pavlidou, C. M. E., and Preuss, H., *Theor. Chim. Acta* **149,** 143 (1978).
61. Becke, A. D., *J. Chem. Phys.* **84,** 4524 (1986).
62. Butcher, K. D., Didziulis, S. V., Briat, B., and Solomon, E. I., *J. Am. Chem. Soc.* **112,** 2231 (1990).

63. Butcher, K. D., Gebhard, M. S., and Solomon, E. I., *Inorg. Chem.* **29,** 2067 (1990).

64. Gebhard, M. S., Deaton, J. C., Koch, S. A., Millar, M., and Solomon, E. I., *J. Am. Chem. Soc.* **112,** 2217 (1990).

65. Gebhard, M. S., Koch, S. A., Millar, M., Devlin, F. J., Stephens, P. J., and Solomon, E. I., *J. Am. Chem. Soc.* **113,** 1640 (1991).

66. Banci, L., Bertini, I., and Luchinat, C., *Struct. Bonding* **72,** 113 (1990).

67. Bertrand, P., and Gayda, J. P., *Biochim. Biophys. Acta* **579,** 107 (1979).

68. Griffith, J. S., *Struct. Bonding* **10,** 87 (1972).

69. McGarvey, B. R., *in* "Transition Metal Chemistry" (R. L. Carlin, ed.), p. 90. Dekker, New York, 1966.

70. Stone, A. J., *Proc. R. Soc. London, Ser. A* **271,** 424 (1964).

71. Geurts, P. J. M., Bouten, P. C. P., and Avoird, A. van der, *J. Chem. Phys.* **73,** 1306 (1980).

72. Dunham, W. R., Bearden, A. J., Salmeen, I. T., Palmer, G., Sands, R. H., Orme-Johnson, W. H., and Beinert, H., *Biochim. Biophys. Acta* **253,** 134 (1971).

73. Münck, E., Debrunner, P., Tsibris, J. C. M., and Gunsalus, I. C., *Biochemistry* **11,** 885 (1972).

74. Anderson, R. E., Dunham, W. R., Sands, R. H., Bearden, A. J., and Crespi, H. L., *Biochim. Biophys. Acta* **408,** 306 (1975).

72. Fukuyama, K., Hase, T., Matsumoto, S., Tsukihara, T., Katsube, Y., Tanaka, N., Kakudo, M., Wada, K., and Matsubara, H., *Nature (London)* **286,** 522 (1980).

76. Dugad, L. B., La Mar, G. N., Banci, L., and Bertini, I., *Biochemistry* **29,** 2263 (1990).

77. Tsukihara, T., Fukuyama, K., Mizushima, M., Harioka, T., Kusunoki, M., Katsube, Y., Hase, T., and Matsubara, H., *J. Mol. Biol.* **216,** 399 (1990).

78. Palmer, G., Dunham, W. R., Fee, J. A., Sands, R. H., Izuka, T., and Yonetani, T., *Biochim. Biophys. Acta* **245,** 201 (1971).

79. Gillum, W. O., Frankel, R. B., Foner, S., and Holm, R. H., *Inorg. Chem.* **15,** 1095 (1976).

80. Petersson, L., Cammack, R., and Rao, K. K., *Biochim. Biophys. Acta* **622,** 18 (1980).

81. Palmer, G., *in* "Iron-Sulfur Proteins" (W. Lovenberg, ed.), p. 285. Academic Press, New York, 1973.

82. Robin, M. B., and Day, P., *Adv. Inorg. Chem. Radiochem.* **10,** 247 (1967).

83. Eaton, W. A., Palmer, G., Fee, J. A., Kimura, T., and Lovenberg, W., *Proc. Natl. Acad. Sci. U.S.A.* **68,** 3015 (1971).

84. Gray, H. B., Siiman, O., and Rawlings, J., *Proc. Natl. Acad. Sci. U.S.A.* **71,** 125 (1974).

85. Mayerle, J. J., Denmark, S. E., Pamphilis, B. V. De, Ibers, J. A., and Holm, R. H., *J. Am. Chem. Soc.* **97,** 1032 (1975).

86. Adzamli, I. K., Kim, H. O. W., Sykes, A. G., and Buxton, G. V., *J. Inorg. Biochem.* **16,** 311 (1982).

87. Jacks, C. A., Bennett, L. E., Raymond, W. N., and Lovenberg, W., *Proc. Natl. Acad. Sci. U.S.A.* **71,** 1118 (1974).

88. Huynh, B. H., Moura, J. J. G., Moura, I., Kent, T. A., LeGall, J., Xavier, A. V., and Münck, E., *J. Biol. Chem.* **255,** 3242 (1980).

89. Day, E. P., Peterson, J., Bonvoisin, J. J., Moura, I., and Moura, J. J. G., *J. Biol. Chem.* **263,** 3684 (1988).

90. Noodleman, L., Case, D. A., and Aizman, A. J., *J. Am. Chem. Soc.* **110,** 1001 (1988).

91. Sontum, S. F., Noodleman, L., and Case, D. A., *in* "The Challenge of d and f Electrons: Theory and Computation" (D. R. Salahub and M. C. Zerner, eds.), p. 366. American Chemical Society, Washington, D.C., 1989.

92. Noodleman, L., Case, D. A., and Sontum, S. F., *J. Chim. Phys.* **86,** 743 (1989).

93. Carter, C. W., *in* "Iron-Sulfur Proteins" (W. Lovenberg, ed.), p. 157. Academic Press, New York, 1977.

94. Noodleman, L., Case, D. A., and Baerends, E. J., *in* "Density Functional Methods in Chemistry" (J. K. Labanowski and J. W. Andzelm, eds.), p. 109. Springer-Verlag, New York, 1991.

95. Aizman, A., and Case, D. A., *J. Am. Chem. Soc.* **104,** 3269 (1982).

96. Noodleman, L., *Inorg. Chem.* **30,** 246 (1991).

97. Moulis, J. M., Lutz, J., Gaillard, J., and Noodleman, L., *Biochemistry* **27,** 8712 (1988).

98. O'Sullivan, T., and Millar, M. M., *J. Am. Chem. Soc.* **107,** 4096 (1985).

99. Sheridan, R. P., Allen, L. C., and Carter, C. W., *J. Biol. Chem.* **256,** 5052 (1981).

100. Papaefthymiou, V., Millar, M. M., and Münck, E., *Inorg. Chem.* **25,** 3010 (1986).

101. Papaefthymiou, G. C., Laskowski, E. J., Frota-Pessoa, S., Frankel, R. B., and Holm, R. H., *Inorg. Chem.* **21,** 1723 (1982).

102. Moulis, J. M., Auric, P., Gaillard, J., and Meyer, J., *J. Biol. Chem.* **259,** 11396 (1984).

103. Gaillard, J., Moulis, J. M., Auric, P., and Meyer, J., *Biochemistry* **25,** 464 (1986).

104. Auric, P., Gaillard, J., Meyer, J., and Moulis, J. M., *Biochemistry* **242,** 525 (1987).

105. Lindahl, P. A., Day, E. P., Kent, T. A., Orme-Johnson, W. H., and Münck, E. J., *Biol. Chem.* **260,** 11160 (1985).

106. Carney, M. J., Papaefthymiou, G. C., Spartalian, K., Frankel, R. B., and Holm, R. H., *J. Am. Chem. Soc.* **110,** 6084 (1988).

107. Collision, D., and Mabbs, F. E., *Chem. Soc., Dalton Trans.,* 1573 (1982).

108. Borshch, S. A., and Chibotaru, L. F., *Chem. Phys.* **135,** 375 (1989).

109. Noodleman, L., *Inorg. Chem.* **30,** 256 (1991).

110. Jordanov, J., Roth, E. K. H., Fries, P. H., and Noodleman, L., *Inorg. Chem.* **29,** 4288 (1990).

111. Noodleman, L., *Inorg. Chem.* **27,** 3677 (1988).

112. Rius, G., and Lamotte, B., *J. Am. Chem. Soc.* **111,** 2464 (1989).

113. Gloux, J., Gloux, P., Hendriks, H., and Rius, G., *J. Am. Chem. Soc.* **109,** 3220 (1987).

114. Patil, D. S., Moura, J. J. G., He, S. H., Teixeira, M., Prickil, B. C., DerVartanian, D. V., Peck, H. D., Jr., LeGall, J., and Huynh, B. H., *J. Biol. Chem.* **263,** 18732 (1988).

115. Ding, X. Q., Bominaar, E., Bill, E., Winkler, H., Trautwein, A. X., Drueke, S., Chaudhuri, P., and Wieghardt, K., *J. Chem. Phys.* **92,** 178 (1990).

116. Conover, R., Park, J.-B., Adams, M. W. W., and Johnson, M. K., *J. Am. Chem. Soc.* **112,** 4562 (1990).

117. Cook, M., and Karplus, M., *J. Chem. Phys.* **83,** 6344 (1985).

118. Coucouvanis, D., *Acc. Chem. Res.* **24,** 1 (1991).

119. Orme-Johnson, W. H., *Annu. Rev. Biophys. Biophys. Chem.* **14,** 419 (1985).

120. Bertrand, P., and Gayda, J. P., *Biochim. Biophys. Acta* **680,** 331 (1982).

121. Mouesca, J. M., Ph.D. thesis, University Joseph Fourier-Grenoble I, France (1991).

122. Mouesca, J. M., Rius, G., and Lamotte, B., *in* "Mixed Valency Systems: Applications in Chemistry, Physics, and Biology (K. Prassides, ed.), p. 431, Kluwer, The Netherlands, 1991.